Chapter 5

Hydro/solvothermal Synthesis of Carbon Dots for Different Applications

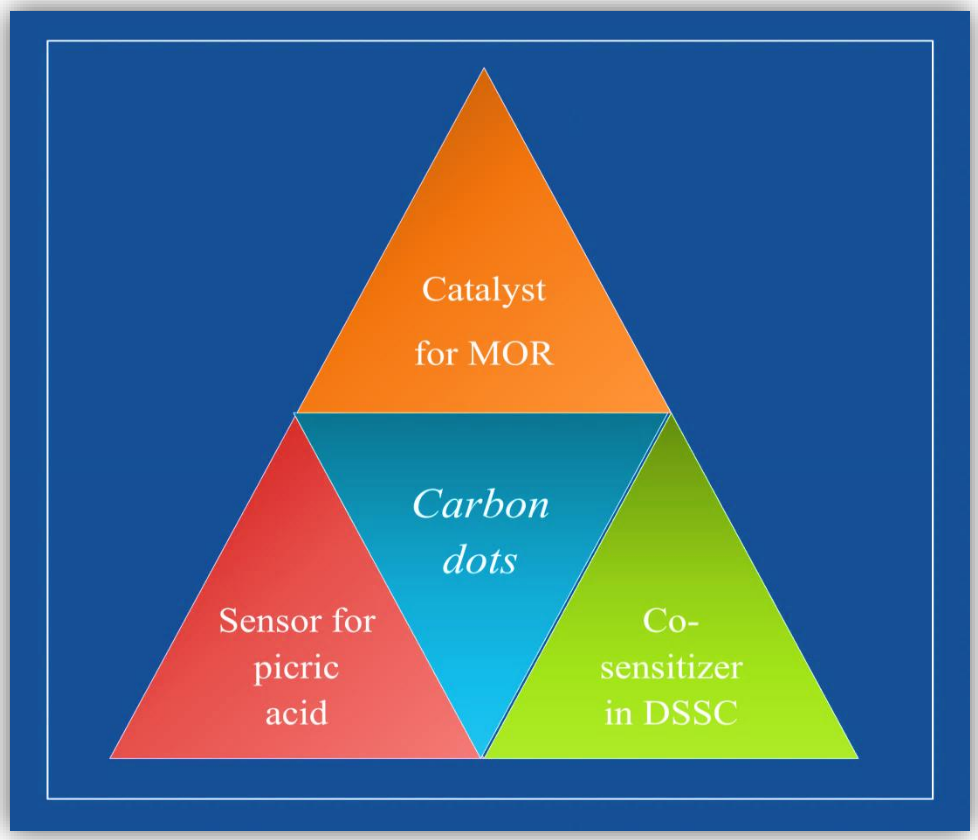

Carbon dots are hydro/solvothermally prepared from two different green carbon sources (*viz.* citric acid and gallic acid) to produce blue and green fluorescence that are eventually used in methanol oxidation reaction, dye sensitized solar cell and 2,4,6-trinitrophenol sensor.

5.1 Introduction

Carbon dots (CDs) are an important class of carbon-based phosphors. Since their discovery in 2004, CDs have attracted tremendous attention as promising alternatives to the toxic, heavy metal based fluorescent semiconductors quantum dots. Use of earth abundant raw materials, excellent biocompatibility, tunable fluorescent properties and good photoinduced electron transport capacity enable their applications in catalytic processes, solar cells and sensors [1–3]. Various attempts have been described in literature for synthesizing CDs with customized properties. For instance, Bhunia*et al.* developed a carbohydrate carbonization method to synthesize carbon nanoparticles exhibiting size-dependent, tunable emissions (blue, green, yellow and red) [4]. They manipulated the nucleation and growth stages by varying the carbohydrate source, reaction temperature and dehydrating agents. Jiang *et al.* introduced a facile solvothermal approach for preparation of CDs by using the three different phenylenediamines isomers (*o*-phenylenediamine, *m*-phenylenediamine and *p*-phenylenediamine) [5]. The CDs emitted red, green and blue colors under a single ultraviolet-light excitation. Zhu *et al.* changed the solvent during solvothermal reaction and obtained CDs with blue, green and red emissions [6]. *N*,*N*-Dimethylformamide (DMF), when used as the solvent medium in solvothermal synthesis, has been reported to produce green emissions. Qu *et al.* stated that when a protic solvent like water is used as the solvent, blue light is emitted. On the other hand, the use of an aprotic medium like DMF results in emission of green light [7]. Du *et al.* used pyrogallic acid as the carbon source to synthesize CDs solvothermally using DMF [8], wherein DMF also served as a nitrogen source for the reaction.

It follows from the above works that longer wavelength emitting CDs can be obtained by increasing their particle size and/or nitrogen content. Taking inspiration from the literature, we have varied the hydro-/solvothermal reaction conditions to produce CDs with different properties. Starting with citric acid as the source of carbon, under hydrothermal conditions blue-emitting CDs are produced. These CDs are used in catalysis of methanol oxidation reaction (MOR) (*Part (a)*). When the solvent is changed from water to DMF, green emitting CDs are obtained using the same carbon source, citric acid. The CDs thus obtained are used in dye sensitized solar cells (DSSCs) (*Part (b)*). Under the same reaction conditions with DMF as the solvent, blue emitting hydrophobic CDs are obtained when gallic acid is used as the carbon source. These CDs are used as the sensing element for detection of 2,4,6-trinitriphenol (TNP) in organic medium (*Part (c)*).

Part (a)

Hydrothermally Synthesized Carbon Dots as Sensitizer for TiO_2 Supported Pt Photo-electrocatalyst for Broadening the Sunlight Response Region in Methanol Oxidation Reaction

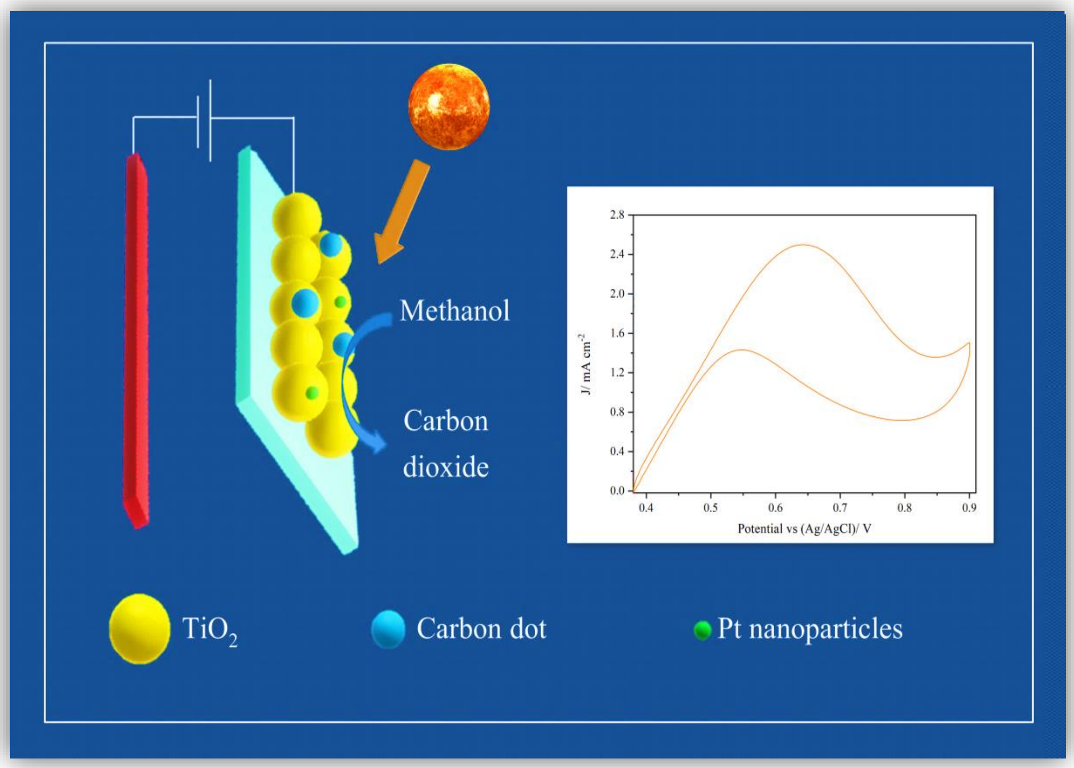

Hydrothermal route is used to prepare blue emitting carbon dots from citric acid having up-conversion property that is used to harness unused visible light and act as sensitizer for TiO_2 supported Pt catalyst in methanol oxidation reaction.

5.2 Introduction

Direct methanol fuel cell (DMFC), employing liquid methanol is a clean power source that converts chemical energy directly into electricity. Development of the anode catalyst constitutes a major facet of this technology. Pt is regarded as the most significant electro-catalyst for MOR in DMFCs [9]. However, Pt nanoparticles have high surface energy which prompts them to aggregate. Additionally, single component Pt electro-catalyst is acutely prone to carbon monoxide (CO) poisoning. MOR follows a dual pathway mechanism, and CO generated as an intermediate in the indirect pathway, strongly adsorb onto the Pt surface. Consequently, the reaction kinetics slows down considerably [10].

Titanium dioxide (TiO_2), on the other hand, is one of the most studied photo-catalysts [11]. The photo-catalytic applications of the wide band gap semiconductor metal oxide are based on the formation of electron-hole pairs when it is irradiated with ultra-violet (UV) light. Combining TiO_2 nanoparticles with Pt nanoparticles presents an effective strategy to develop a photo-electrocatalyst, wherein MOR is photo-catalyzed by the photo-induced holes on the TiO_2 nanoparticles and electro-catalyzed by the Pt nanoparticles at the same time. Previous works show that such a scenario can lead to better catalytic activities by the composites [12,13]. High surface area TiO_2 nanoparticles not only act as a support for homogeneous dispersion of the Pt nanoparticles on its surface and reduce the Pt loading, but also help in mitigating the CO poisoning effect.

However, TiO_2 can be photo-excited only by the UV part of the solar light, which accounts for about 4% of the total solar light reaching the earth’s surface. So, there is a huge scope for developing new innovative catalyst designs, which can extend the sunlight absorption stretch to the visible region. Some of the popular routes include doping TiO_2 with different ions, coupling with small band gap semiconductors, sensitizing with organic dyes, and so on [14–16]. CDs, with excellent charge transfer ability, has already been reported as a sensitizer for TiO_2 nanoparticles,and the visible light active catalyst thus produced has been used in photo-degradation, solar cells and water-splitting, etc. [1,2,17] . In addition, CDs also possess an

---

This part of the thesis is published in:

Bora, A., Mohan, K., Doley, S., Goswami, P., and Dolui, S. K. Broadening the sunlight response region with carbon dot sensitized TiO_2 as a support for a Pt catalyst in the methanol oxidation reaction. *Catalysis Science & Technology*, 8(16):4180-4192, 2018.

exceptional ability to offer resistance to CO poisoning on Pt surface, thereby enabling better performances by Pt based catalysts in MOR [18–20]. Recently, Zheng *et al.* reported an interesting result where they observed that CD sensitized Pt@Bi_2WO_6/FTO electrode showed better catalytic activity and stability in MOR in comparison to the non-sensitized electrode [21]. The sensitization by CDs broadened the photo-response range of Bi_2WO_6 and also created a new type of CD-Pt catalyst. They further suggested that CO molecules are preferentially adsorbed on CDs, which leaves the Pt sites free. Hydroxyl radicals ($^{\bullet}OH$) generated during the catalysis process can oxidize the CO molecules, a fact that has also been stated by Zhai*et al.*[22]. Following this vision, we report a novel photo-electrocatalyst: Pt supported on CD sensitized TiO_2 nanoparticles(Pt/CD/TiO_2). The nanocomposite performs the dual function of a photo-catalyst and an electro-catalyst under simulated solar light illumination. The presence of TiO_2 and CD lead to comprehensive exploitation of both the UV and visible region of the solar spectrum, in addition to acting as anti-CO poisoning mediators.

5.3 Materials and methods

5.3.1 Chemicals

Citric acid, ethylenediamine, TiO_2, terephthalic acid, chloroplatinic acid (H_2PtCl_6), sodium borohydride ($NaBH_4$), sodium hydroxide (NaOH), quinine sulfate (QS), potassium ferricyanide ($K_3[Fe(CN)_6$) and potassium ferrocyanide ($K_4[Fe(CN)_6]$) were purchased from Merck. Methanol (CH_3OH) and sulfuric acid (H_2SO_4) were also procured from Merck. Distilled water was used for all purposes.

5.3.2 Synthesis of CDs

Hydrothermal route was applied to synthesize the CDs by following the synthesis process reported by Zhu *et al.* was used [23]. In a typical procedure, 0.42 g citric acid and 0.54 mL of ethylenediamine were dissolved in 10 mL distilled water. The reaction mixture was then transferred to a Teflon lined autoclave and heated at 150 ºC for 5 h. The autoclave was allowed to cool down to room temperature. A transparent, brownish black liquid was obtained, which was subjected to centrifugation and filtration with a 0.22 µm membrane, and rotary evaporation to obtain powdered CDs.

5.3.3 Synthesis of platinized CDx/TiO_2 composites

Synthesis of platinized CDs/TiO_2 was carried out in two steps, as summarized in **Scheme 5.1**.

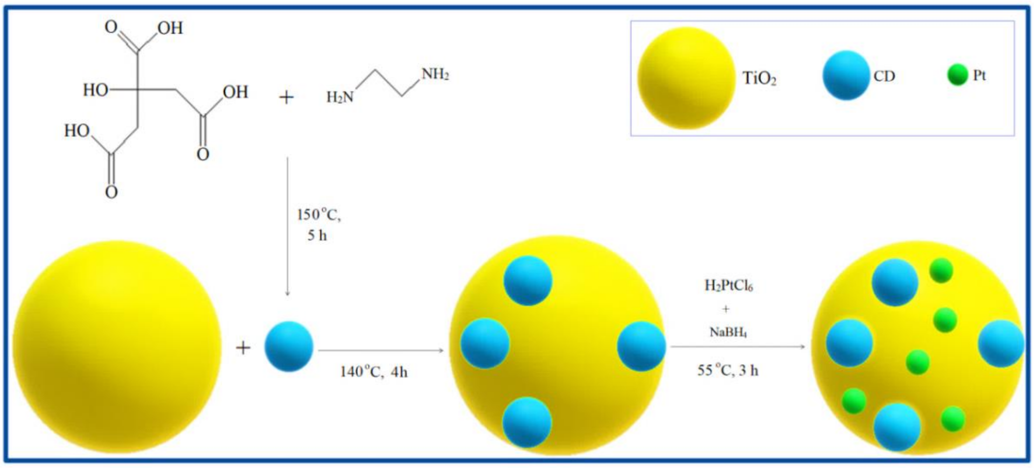

Scheme 5.1 Schematic representation of the steps involved in the synthesis of Pt/CD/TiO_2.

Step 1: Synthesis of CD sensitized TiO_2 nanoparticles

Hydrothermal route was again employed for producing CD sensitized TiO_2 nanoparticles (CD/TiO_2) following the procedure reported by Yu *et al.* [24]. A series of nanocomposites with different weight percentages (wt%) of CDs were prepared to study the effect of the CD content on MOR. The nanocomposites were labelled as CD0/TiO_2, CD1/TiO_2, CD2/TiO_2 and CD3/TiO_2 with CD contents of 0, 1, 2 and 3 wt% respectively. In general, 0.4 g of TiO_2 nanoparticles (~ 21 nm size) were dispersed in 6 mL ethanol and a 2 mg mL^{-1} aqueous solution of CD (according to the wt%) was added to it. 10 mL distilled water was further added to the reaction mixture and stirred for 4 h at room temperature. It was then transferred to a Teflon lined autoclave and heated at 140 ºC for 4 h. Once the autoclave cooled down to room temperature, the reaction product was centrifuged and vacuum dried to obtain brownish-white CD*x*/TiO_2powders (*x* denotes the content of CD).

Step 2: Platinization of CDx/TiO_2 composites

For platinization of CD*x*/TiO_2, a chemical reduction route was employed as mentioned by Pan *et al*. with slight modifications [20]. In this process, 50 mg of CD*x*/TiO_2 powder was dispersed in 10 mL distilled water. Then an aqueous solution of 20 mM H_2PtCl_6 (corresponding to *y* wt % Pt; *y* = 2.5, 3.0, 3.5 and 4.0) was added drop-wise to the above dispersion with stirring. For instance, to prepare the 3.0 wt% platinized composite Pt3/CD2/TiO_2, 1.67 mL H_2PtCl_6 solution was added to the 5 mg mL^{-1} CD2/TiO_2 dispersion. To this reaction mixture, 1 mL of the aqueous solution of 50 mM $NaBH_4$ was added drop-wise. Prior to that, the pH of $NaBH_4$ solution was adjusted to 12 by adding NaOH. The resulting solution was continuously stirred for 3 h at 55 ºC. Finally, the solution was filtered, washed with de-ionized water and the solvent evaporated with a rotavapor to obtain Pt3/CD2/TiO_2 powder.

5.3.4 Characterization

The instruments used for obtaining Fourier transform infra-red (FTIR) spectra, UV-visible spectra, powder X-ray diffraction (XRD) patterns, X-ray photoelectron (XPS) spectra and transmission electron microscopy (TEM) images of the samples are previously described. Additionally, the fluorescence emission spectra of the materials were recorded on a Hitachi F-2700 fluorescence spectrophotometer. A JEOL JSM-6390 LV scanning electron microscope was used to obtain the energy dispersive X-ray spectroscopy (EDX) data of the CDs. All the electrochemical measurements were performed on a Bio-Logic SP-150 potentiostat.

5.3.5 Quantum yield measurement

Five different concentrations each of three different types of CDs and QS were prepared in distilled water (refractive index (η) = 1.33) and 0.1 M H_2SO_4 (η = 1.33) respectively. The UV-visible absorbance intensities and the PL intensities of all the samples were recorded at their excitation wavelengths (340 nm). The literature value of the quantum yield of QS (Φ_{QS}) is 0.54. The integrated PL intensities of each sample at different concentrations were plotted against their corresponding absorbance values. From the slopes of the plotted lines (s), the quantum yield of CDs (Φ_{CD}) was calculated by using **relation (5.1)** [24].

$$\Phi_{CD} = \Phi_{QS}(s_{CD} \;/\; s_{QS})(\eta^2_{water} \;/\; \eta^2_{0.1\ M\ H_2SO_4}) \quad \textbf{(5.1)}$$

5.4 Results and discussion

In this study, hydrothermal route was selected to prepare CDs using citric acid as the carbon source.

5.4.1 FTIR spectra analyses. The FTIR spectra of hydrothermally synthesized CDs and CD/TiO_2 nanocomposites are shown in **Figure 5.1**. For the CDs, the broad peak (3000-3700 cm^{-1}) is attributed to the vibration of –OH bond while the one at 2943 cm^{-1} is associated with –CH vibration. The peaks at 1658, 1558 and 1422 cm^{-1} are ascribed to –C=O, –C=C, and –NH groups respectively [25].Similar characteristic peaks are also seen in CD/TiO_2, affirming the incorporation of CDs in the TiO_2 matrix. Additionally, another broad peak appears in the region below 1000 cm^{-1}. This region is typically allotted to Ti–O–Ti vibrational peak whereas the peak for Ti–O–C bond is generally observed around 800 cm^{-1}. Hence, the broad peak can be visualized as a combination of both these groups, implying the formation of Ti-O-C chemical bond between the residual carboxylic groups of CDs and surface hydroxyl groups of TiO_2[26].

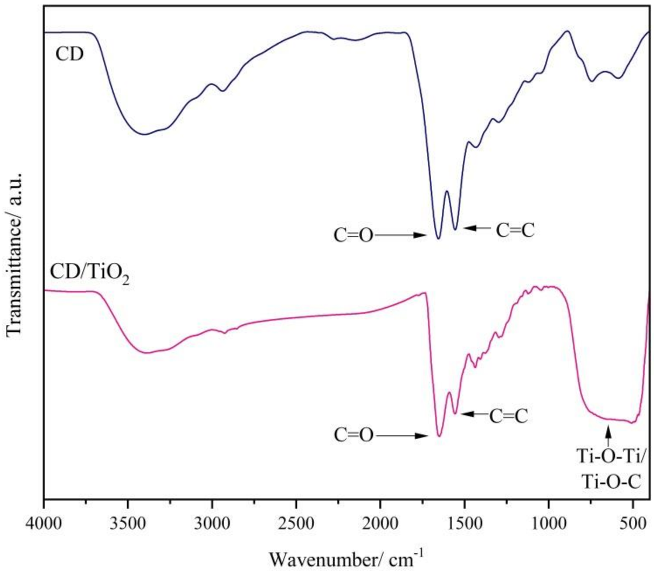

Figure 5.1 FTIR spectra of CD and CD/TiO_2 nanocomposite.

5.4.2 XPS analyses. XPS was used to determine the elemental composition of the

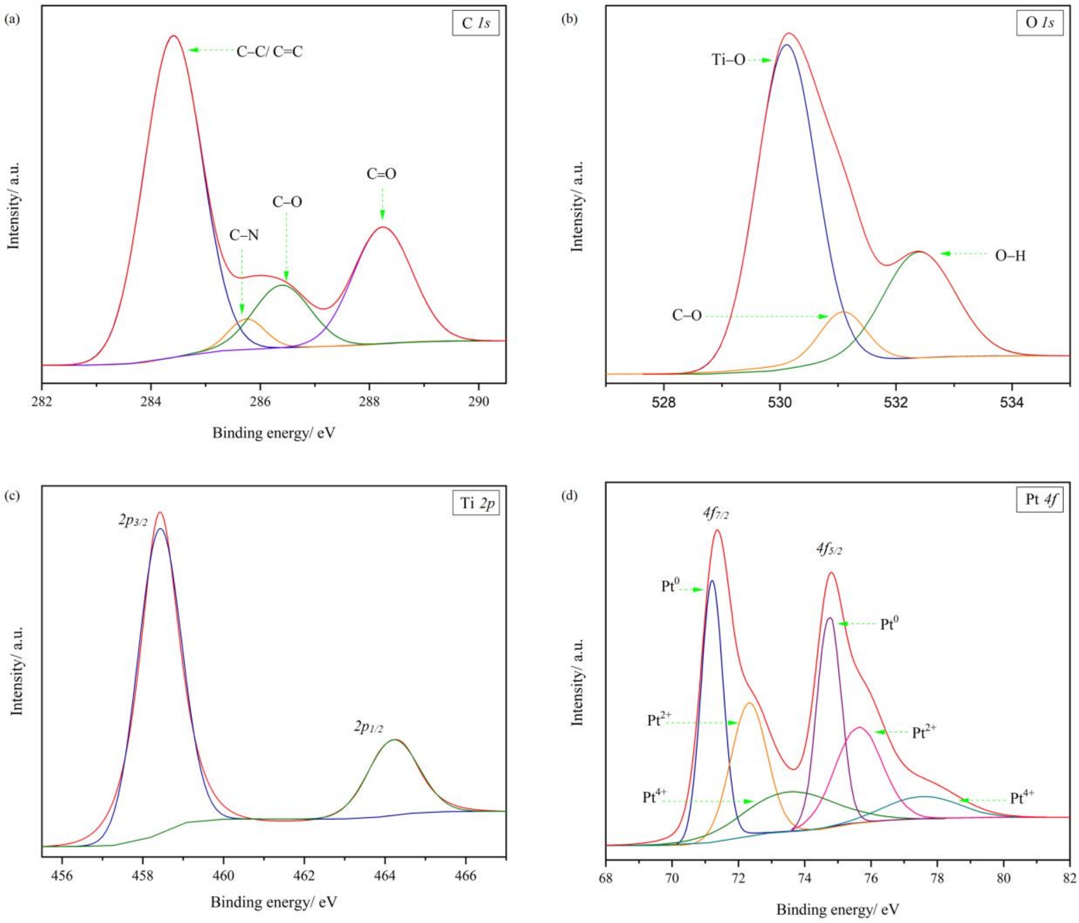

Figure 5.2 Core-level XPS patterns of **(a)** C *1s*, **(b)** O *1s*, **(c)**Ti*2p* and **(d)** Pt *4f* for Pt/CD/TiO_2 nanocomposite.

prepared Pt/CD/TiO_2 nanocomposite. The typical high-resolution XPS spectra for C *1s*, O *1s*, Ti*2p* and Pt *4f* showing the peaks at their respective binding energies are displayed in **Figure 5.2.** In the deconvulated spectrum of C *1s*, four well-resolved peaks are seen which can be ascribed to the following different C functional groups: C–C/ C=C (284.4 eV), C–N (285.7 eV), C–O (286.4 eV) and C=O (288.2 eV) [27]. The core-level O *1s* spectrum reveals the existence of three individual peaks at 530.1, 531.1 and 532.4 eV corresponding to Ti–O, C–O and O–H bonds respectively [24]. The high resolution Ti*2p* spectrum consists of two peaks: Ti ($2p_{3/2}$) at 458.4 eV and Ti ($2p_{1/2}$) at 464.2 eV. The XPS spectrum in the Pt *4f* region divulges the existence of doublet at 71.2 eV (Pt $4f_{7/2}$) and 74.7 eV (Pt $4f_{5/2}$), validating the presence of Pt in (0) oxidation state. In addition, the spectrum also shows peaks having (+2) and (+4) oxidation states at 72.3 eV (Pt $4f_{7/2}$) and 75.7 eV (Pt $4f_{5/2}$), and 73.6 eV (Pt $4f_{7/2}$) and 77.6 eV (Pt $4f_{5/2}$) respectively. Pt(0) is considered to be the active site for methanol adsorption while Pt(+2) can promote the oxidation of CO_{ads}into CO_2 [28].

5.4.3 XRD analyses. The XRD pattern of the Pt/CD/TiO_2 nanocomposite shows the co-existence of anatase and rutile phases of TiO_2, although it is mainly composed of the anatase phase (**Figure 5.3**). Nine characteristic peaks of anatase TiO_2 can be seen including the most remarkable one at $2\theta = 25.2^{\circ}$ due to the (101) plane. Three distinctive peaks at 2θ values of 27.4°, 36.1° and 56.6° corresponds to the (110), (101) and (220) planes of rutile TiO_2. The XRD pattern of the hydrothermally produced CDs from citric acid emphasizes their amorphous nature (**Figure 5.3 inset**). The primary diffraction peak is quite broad and centered around $2\theta = 22.3^{\circ}$, while another broad peak is seen at $2\theta = 40.7^{\circ}$. These peaks correspond to the (002) and (100) planes of the graphitic framework respectively [29]. The broad nature of the peaks indicates the highly

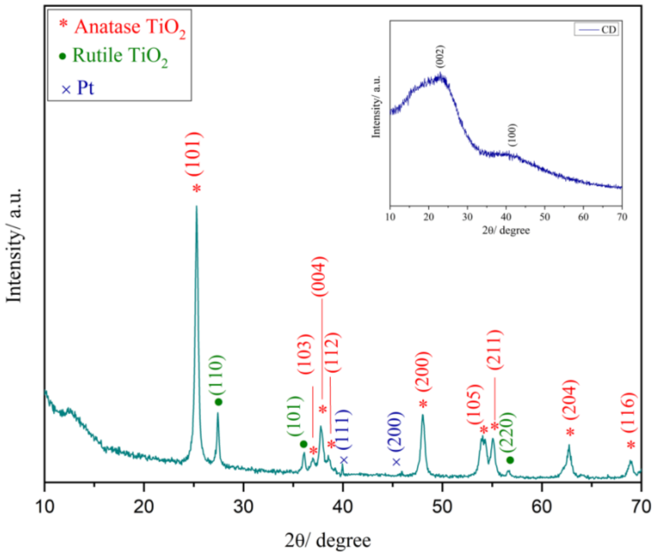

Figure 5.3 XRD pattern of Pt/CD/TiO_2 nanocomposite (inset: XRD pattern of CD).

disordered structure of CDs. In the XRD pattern of the nanocomposite, however, no diffraction peak pertaining to the CDs is visible. This can be attributed to amount of CD added being very less and its low crystallinity. Two additional low intensity peaks at $2\theta = 40.0^{\circ}$ and 46.0° are also seen in the XRD pattern, corresponding to the (111) and (200) planes of Pt respectively [52]. The incorporation of CDs and Pt nanoparticles show no noticeable influence on the crystallinity or the phase of TiO_2.

5.4.4 Morphological study.Figure 5.4 (a) and **(b)** display the TEM images of the Pt/CD/TiO_2 nanocomposite. With TiO_2 as a support, CDs and Pt nanoparticles are seen randomly distributed over the surface without any aggregation. The typical size of the acquired TiO_2 nano-powder is less than 21 nm, and shows good crystalline nature. Most of the particles exist in anatase phase with a lattice spacing of 0.33 nm obtained from the high resolution TEM (HRTEM) micrograph of TiO_2 **(Figure 5.4 (c))**. This lattice spacing represents the interlayer distance of the (101) crystal plane of TiO_2 [31]. The CDs, on an average, have spherical morphology with a diameter of 6 nm. The CD nanoparticles are predominantly amorphous in nature. Chemically reduced Pt nanoparticles, on the other hand, have a typical size of 3 nm. The HRTEM image reveals 0.22 nm lattice spacing corresponding to the (111) Pt crystal plane **(Figure 5.4 (d))**[32].

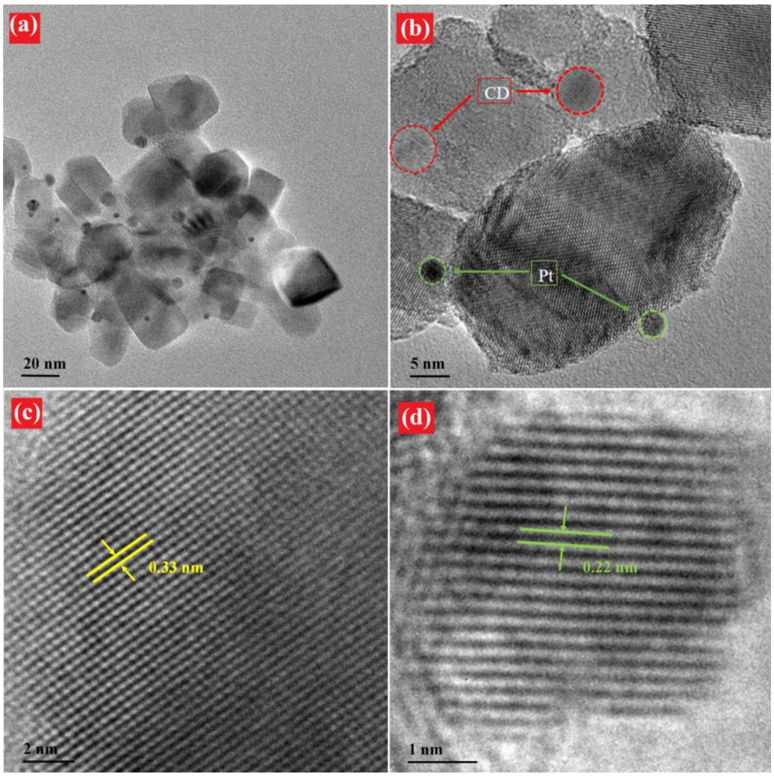

Figure 5.4 (a, b) TEM micrographs of Pt/CD/TiO_2 nanocomposite, and **(c, d)** HRTEM images of TiO_2 and Pt.

5.4.5 EDX analyses. The EDX elemental mapping results for the Pt based nanocomposite are presented in **Figure 5.5**. The analysis confirms the presence of Ti, C and Pt resulting from TiO_2, CDs and Pt nanoparticles. A denser distribution of Ti than the other two elements signifies that C and Pt are uniformly distributed on the surface of TiO_2.

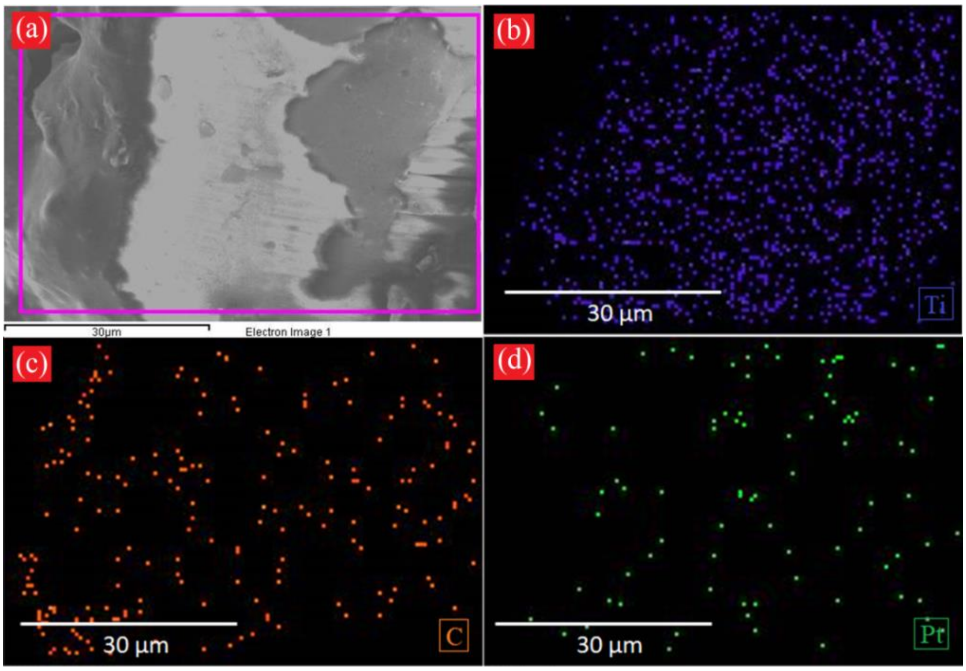

Figure 5.5 Elemental mapping images of Ti, C and Pt.

5.4.6 Optical properties.Figure 5.6 (a) shows the UV–visible absorption spectra of CDs, TiO_2 and CD/TiO_2 nanocomposites in the range 210-700 nm. Two absorption bands peaking at 235 nm and 338 nm are the prominent features of the spectrum of CDs. In accordance with previous reports, the peak at 235 nm is observed due to π-π* transition of aromatic C=C bonds while the one at 338 nm is attributed to n-π* transitions of C=O [33,34]. In case of TiO_2 nanoparticles, a monotonous increase in absorbance from the visible region to the UV region is seen, with the appearance of a broad peak corresponding to 3.18 eV optical band gap ($E_{g,op}$), which matches with the anatase form of TiO_2 [35]. **Figure 5.6 (b)** shows the Tauc's plots ($(\alpha h\nu)^{1/2}$ vs. photon energy $(h\nu)$) of the nanomaterials [36], according to the following dependence **(relation (5.2))**:

$$\alpha h\nu = (h\nu - E_{g,op})^{1/p} \qquad \textbf{(5.2)}$$

whereα and p represent the absorption coefficient and the power coefficient (=1/2) of indirect allowed electronic transitions respectively. With the modification of TiO_2 with CDs, the $E_{g,op}$ value narrows down to 3.08 eV, which can be attributed to the formation of Ti–O–C bond. This suitably explains the extension of solar light harnessing potential to the visible range for attaining more efficient activity by the CD/TiO_2 nanocomposites.

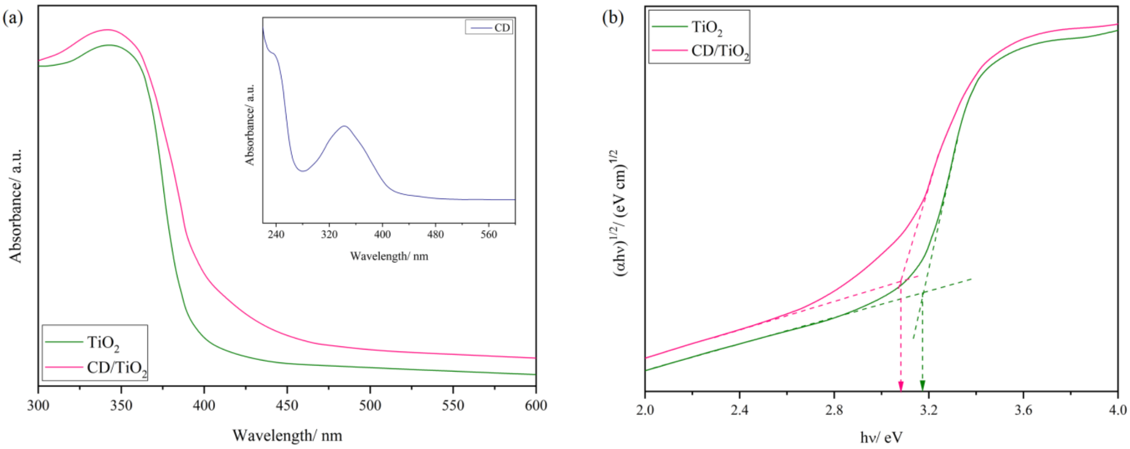

Figure 5.6 (a) UV-visible absorption spectra of CD, TiO_2 and CD/TiO_2 nanocomposite, and **(b)** their corresponding Tauc's plots for optical band gap determination.

To verify the fluorescence property of the CDs, the nanoparticles were dispersed in distilled water and their PL spectra were recorded at different excitation wavelengths as shown in **Figure 5.7**. As expected, the CDs display excitation dependent fluorescent properties with a progressively red-shift when excited from 300 nm to 500 nm at an interval of 50 nm. Although a bit controversial, this phenomenon is mostly related to the presence of surface traps in the radiative transition process [37]. Trapping states with varying energy levels are established by

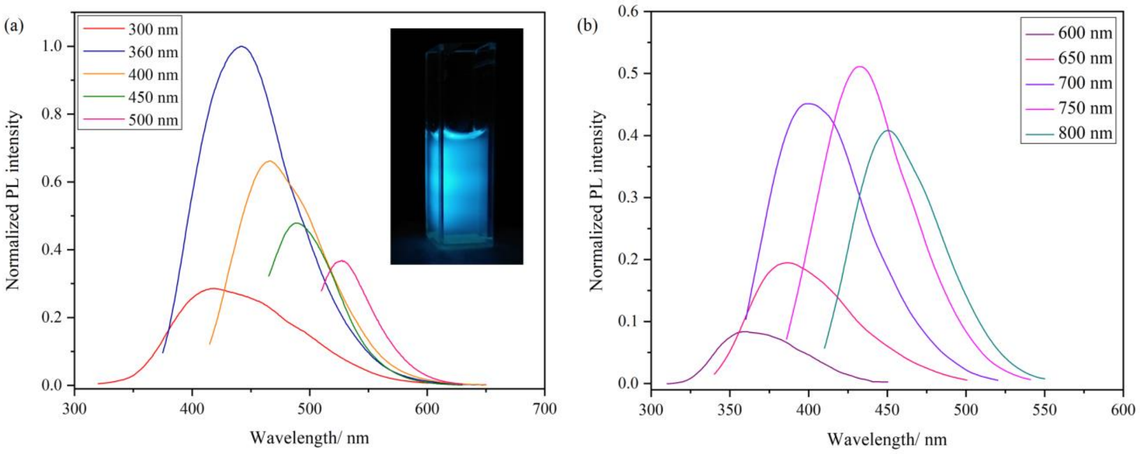

Figure 5.7 (a) Down-converted PL spectra of CDs at different excitation wavelengths (inset: a digital photograph of blue coloured emission for CDs excited at 360 nm) and **(b)** up-converted PL spectra of CDs.

the different oxygen surface functional groups (C–O and C=O) present in the CDs. Hence, by varying the excitation energy, the fluorescence emission can be changed. The maximum intensity emission peak is obtained at 442 nm, associated with blue coloured fluorescence (29% quantum yield **(Figure 5.8)**). **Figure 5.7 (a, inset)** shows the corresponding digital photograph of water dispersed CDs at an excitation wavelength of 360 nm. Interestingly, as shown in **Figure 5.7 (b)**,the CDs also display exceptional up-conversion PL properties. When excited by long-wavelength light (600nm - 800 nm), the up-converted emission peaks appear in the range from 360 nm to 450 nm. Multi-photon active process has been reported to be the main reason for this occurrence, a process in which two or more photons are concurrently absorbed resulting in a shorter wavelength emission in comparison to the longer wavelength excitation (anti-Stokes type emission) [38].

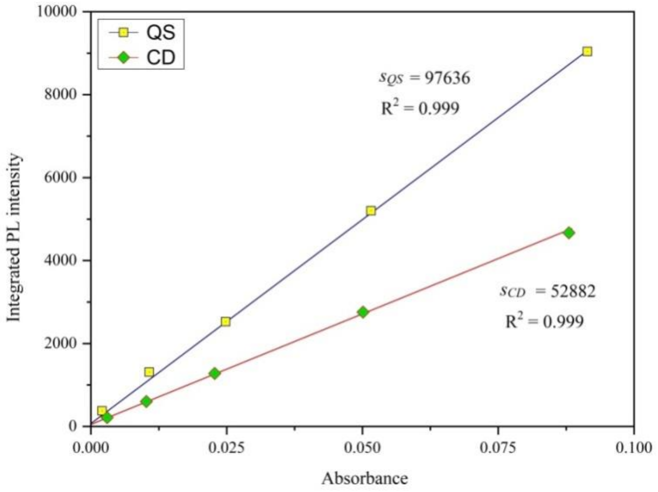

Figure 5.8 Photoluminescence *vs.* absorbance plots of CD and QS.

5.4.7 Photo-electrocatalytic activity of CD sensitized TiO_2 supported Pt nanocomposites. Fluorine doped tin oxide (FTO) coated glass slides were used as substrates for all the photo-electrochemical measurements. A paste of 10 mg mL^{-1} Pt*y*/CD*x*/TiO_2 paste in ethanol was prepared ultrasonically. It was then coated onto 1 cm^2 surface area of the glass slides *via* doctor blade technique and sintered at 400 ºC for 30 min. The resulting glass slides were used as working electrodes.

As a preliminary step towards exploring the catalytic activity of Pt supported on CD sensitized TiO_2 for MOR, its presence was assessed by CV measurements. The cyclic voltammograms were acquired in an electrolyte solution comprising of 0.5 M H_2SO_4 at a scan rate of 20 mV s^{-1}. Characteristic hydrogen adsorption/desorption peaks can be seen along with Pt oxidation and Pt oxide reduction peaks in **Figure 5.9**, affirming the presence of Pt in the composite catalysts. The electrochemical active surface areas (EASAs) of the Pt based catalysts are determined by integrating the area of hydrogen adsorption/ desorption peaks of the CV curves. Assuming that Pt requires 0.21 mC cm^{-2} electrical charge for monolayer adsorption/desorption of hydrogen, the EASA can be estimated by **relation (5.3)**.

$$EASA = \frac{q_H}{0.21 \times m_{Pt}} \quad \textbf{(5.3)}$$

whereq_H is the electrical charge of hydrogen adsorption/ desorption obtained from the integrated CV peak area after double layer correction and m_{Pt} is the Pt loading on the working electrode.The EASA of Pt3/CD2/TiO_2 catalyst is estimated to be 88.49 m^2 $g^{-1}{}_{Pt}$ while that of Pt3.5/TiO_2, calculated in similar way, is 65.86 m^2 $g^{-1}{}_{Pt}$. This suggests that the electrochemical accessibility of Pt3/CD2/TiO_2 is much better than that of Pt3.5/TiO_2, which is a crucial requirement for MOR. The electrical conductivity is an important parameter that affects EASA [39]. CDs prepared from citric acid have been previously reported to be conducting in nature [40].The higher conductivity of Pt3/CD2/TiO_2 (0.7 S m^{-1}) in comparison to Pt3.5/TiO_2 (0.05 S m^{-1}) due to the presence of CDs facilitates the transfer of electrons and also fastens the mass-transfer kinetics at the surface of the electrode, resulting in a larger EASA.

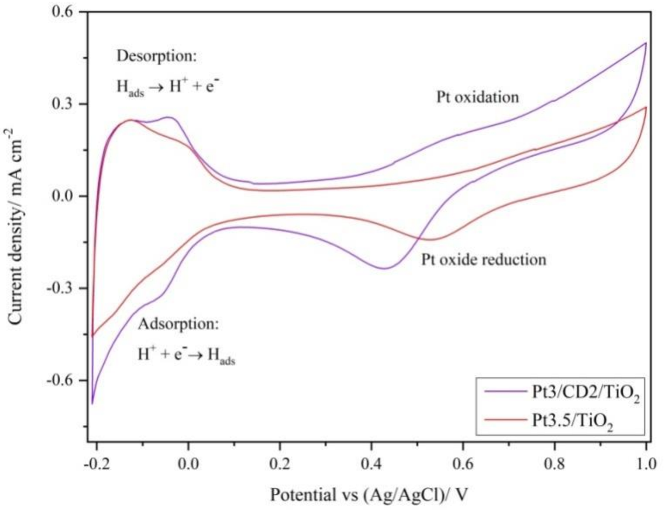

Figure 5.9 Cyclic voltammograms of Pt3/CD2/TiO_2 and Pt3.5/TiO_2catalysts measured in 0.5 M H_2SO_4 aqueous electrolyte.

Figure 5.10 (a) shows a representative set of CV profiles for TiO_2 supported Pt before and after simulated solar light illumination, measured in an electrolytic solution of 0.5 M CH_3OH and 0.5 M H_2SO_4. The anodic peak in the forward scan appearing at approximately 0.63 V is generally considered the primary peak of MOR. A second anodic peak also appears during the backward scan at around 0.53 V. Goodenough's team was the first to accredit this peak to the oxidation of residual intermediate carbon species like CO [41]. CO poisoning is highly detrimental to the performance of a catalyst, hence it is beneficial to evaluate the susceptibility of the catalyst towards it. Following the work of Goodenough, many researchers have since then reported that the CO tolerance can be determined from the ratio of the forward scan peak current (I_f) to the backward scan peak current (I_b) [42]. From this definition, it can be interpreted that a smaller value of I_b, i.e., a higher I_f/I_bratio, indicates that CO like intermediates are eliminated to a great extent during the forward scan. In the case of TiO_2 supported Pt catalysts, an increased current response is observed in terms of the two peaks when it is under irradiation. The peak current densities of Pt*y*/CD0/TiO_2 (or denoted simply as Pt*y*/TiO_2 since the amount of CD is zero) composites are listed in the form of a bar diagram in **Figure 5.10 (b)**. The photo-electrocatalyst Pt3.5/TiO_2 shows the best performance with an $I_f$value of 1.16 mA cm^{-2}, which is an increase of 24% from the condition when no light source is present.

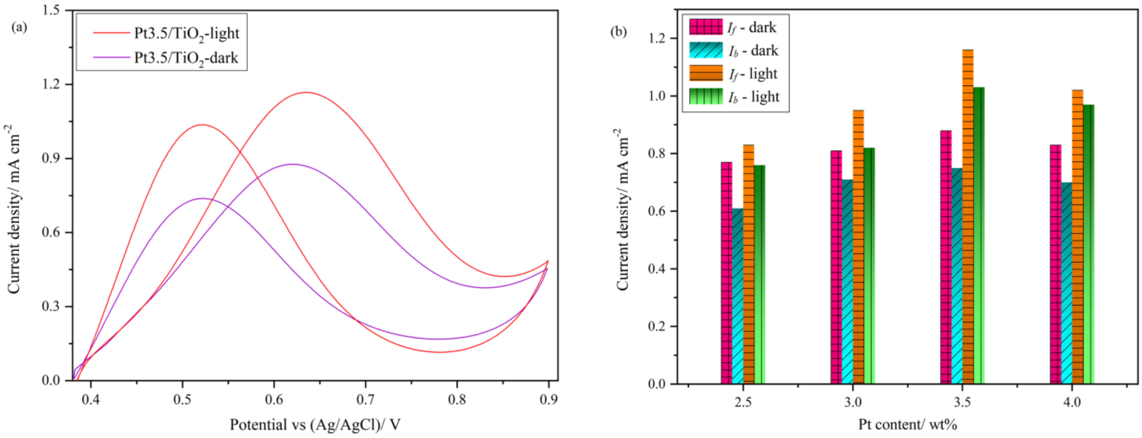

Figure 5.10 (a) A representative set of CV profiles of Pt3.5/TiO_2catalyst measured in 0.5 M CH_3OH + 0.5 M H_2SO_4 electrolyte in the presence and absence of simulated solar lightirradiation, and **(b)** bar diagrammatic representation of the forward and backward current densities for different compositions of Pt*y*/TiO_2 catalysts under dark and light conditions.

The contribution to the catalytic activity of Pt*y*/TiO_2 comes from two different processes of both the components occurring concurrently. Pt acts as an electro-catalyst in the MOR, and is involved in stripping off of four hydrogen atoms of methanol through a set of reactions which ultimately releases CO_2 [43]. The reactions described in **relations (5.4 (a)-(d))** occur on the Pt surface sites (Pt_S), causing chemisorption of CO molecules.

$$CH_3OH + Pt_S \rightarrow Pt_S - CH_2OH + H^+ + e^- \qquad \textbf{(5.4 (a))}$$

$$\mathrm{Pt_S - CH_2OH \rightarrow Pt_S - CHOH + H^+ + e^-} \qquad \textbf{(5.4 (b))}$$

$$\mathrm{Pt_S - CHOH \rightarrow Pt_S - COH + H^+ + e^-} \qquad \textbf{(5.4 (c))}$$

$$\mathrm{Pt_S - CHOH \rightarrow Pt_S - CO + H^+ + e^-} \qquad \textbf{(5.4 (d))}$$

Now, the conversion of this chemisorbed CO to CO_2 is a crucial step in the MOR. Initially proposed by Gilman, the electrochemical oxidation of CO to CO_2 follows a “reactant-pair” mechanism [44]. This now-accepted mechanism to release CO_2 follows a Langmuir-Hinshelwood type reaction between CO and a hydroxyl moiety (–OH) produced by the oxidation of water on an adjacent site (**relations (5.4 (e)** and **(f))**).

$$\mathrm{Pt_S + H_2O \rightarrow Pt_S - OH + H^+ + e^-} \qquad \textbf{(5.4 (e))}$$

$$\mathrm{Pt_S - OH + Pt_S - CO \rightarrow 2Pt_S + CO_2 + H^+ + e^-} \qquad \textbf{(5.4 (f))}$$

TiO_2, on the other hand, serves as a photo-catalyst in MOR. The photo-oxidation of methanol generally proceeds *via*hydroxymethyl radical ($^\bullet CH_2OH$) formation resulting in the release of CO_2 [45,46]. Under UV light irradiation, free electrons and holes are generated within the conduction band (CB) and valence band (VB) respectively (**relation (5.5 (a))**). The holes then reach the surface of TiO_2 and are trapped at the band gap surface states. They may then react with terminal OH^- groups to generate hydroxyl radical ($^\bullet OH$) (**relation (5.5 (b))**), which assist in the oxidation of non-adsorbed methanol to $^\bullet CH_2OH$ radical (**relation (5.5 (c))**). Alternatively, the holes can also oxidize the adsorbed methanol to $^\bullet CH_2OH$radical (**relation (5.5 (d))**). In the presence of oxygen, a series of reactions takes place terminating with the release of CO_2 (**relations (5.5 (e)-(g))**).

$$\mathrm{TiO_2 + h\nu(\geq E_g) \rightarrow h^+_{Valence\ band} + e^-_{Conduction\ band}} \qquad \textbf{(5.5 (a))}$$

$$\mathrm{OH^- + h^+_{Valence\ band} \rightarrow \bullet OH} \qquad \textbf{(5.5 (b))}$$

$$\mathrm{(CH_3OH)_{sol} + \bullet OH \rightarrow CH_2OH^\bullet + H^+} \qquad \textbf{(5.5 (c))}$$

$$\mathrm{(CH_3OH)_{ads} + h^+_{Valence\ band} \rightarrow \bullet CH_2OH + H^+} \qquad \textbf{(5.5 (d))}$$

$$\mathrm{\bullet CH_2OH + O_2 \rightarrow HCHO + O_2^{-\bullet} + H^+} \qquad \textbf{(5.5 (e))}$$

$$\mathrm{HCHO + {}^1\!/_2\, O_2 \rightarrow HCOOH} \qquad \textbf{(5.5 (f))}$$

$$\mathrm{HCOOH + {}^1\!/_2\, O_2 \rightarrow CO_2 + H_2O} \qquad \textbf{(5.5 (g))}$$

TiO_2 is a *n*-type semiconductor and with the loading of Pt, a Schottky barrier is formed at their interface [47,48]. Recombination of photo-generated electrons and holes is suppressed within the space charge region by the large electric field, which helps in the migration of electrons from TiO_2 to Pt, with Pt acting as an electron scavenger. With the increase in the loading of Pt, the space charge region becomes increasingly narrower. Consequently, the catalytic activity increases till an optimum composition is obtained with 3.5 wt% Pt content as is evident from **Figure 5.10 (b)**. At this particular Pt loading, the thickness of the space charge region can be considered approximately equal to the penetration depth of the photons. However, with further increase in Pt content, the space charge layer becomes too narrow such that the photon penetration depth exceeds its thickness. In that case, recombination of electron-hole pairs become much easier and the catalytic activity deteriorates.

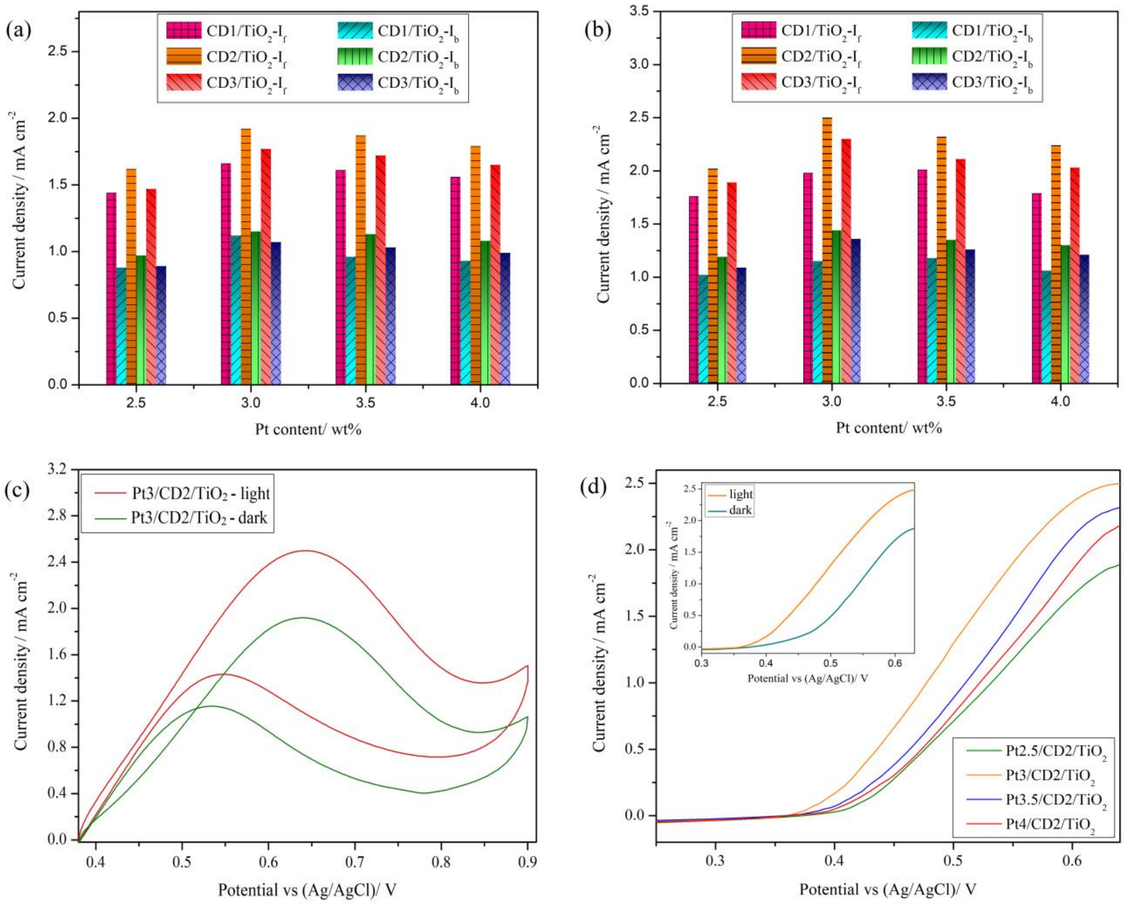

Figure 5.11 Bar diagrammatic representation of I_f and I_b for different compositions of Pt*y*/CD*x*/TiO_2 catalysts under **(a)** light and **(b)** dark conditions, **(c)** a representative set of CV profiles of Pt3/CD2/TiO_2measured in 0.5 M CH_3OH + 0.5 M H_2SO_4 electrolyte in the absence and presence of simulated solar lightirradiation and **(d)** LSV curves of the Pt*y*/CD2/TiO_2 composite under irradiation of light (The plots in the inset show the influence of light on Pt3/CD2/TiO_2 catalyst's behavior).

The current densities for different compositions of the composite (Pt*y*/CD*x*/TiO_2) with variation in Pt content are shown in **Figure 5.11 (a)** and **(b)**. The highest $I_f$value is attained with the Pt3/CD2/TiO_2 catalyst (2.50 mA cm^{-2}) in the presence of solar light simulation. This value is considerably higher than the value obtained with Pt3.5/TiO_2 as well as Pt3/CD2/TiO_2 under dark conditions. **Figure 5.11 (c)** shows another set of CV curves for MOR when the TiO_2 supported Pt catalyst is sensitized by CDs. The I_f and I_b values show considerable increase than those obtained prior to CD sensitization. The role of CD can be suggested to be two-fold in this case: as alleviation of CO poisoning and sensitizing TiO_2 nanoparticles to the visible solar light spectrum *via* up-conversion phenomenon. With regard to monitoring the CO poisoning effect on Pt catalytic sites, considering I_f/I_b as an indicator, an increase in its value with the addition of CDs is clearly seen. For TiO_2 supported Pt (Pt3.5/TiO_2), this value is 1.13. On sensitizing with CDs (Pt3/CD2/TiO_2), this value rises to 1.75. A couple of possibilities have been suggested for the CO poisoning alleviating effect by CDs. For instance, Pan *et al.* have mentioned an alternate route for water activation on the surface of CDs to form chemisorbed hydroxyl groups, which inturn speed up the oxidation of the chemisorbed CO [20]. CO_2 is formed as a product, thereby cleaning up the Pt surface for further MOR (**relations (5.6 (a), (b))**). This process is quite similar to the one occurring on the TiO_2 surface that has been reported by Chen *et al.*, wherein TiO_2 promotes the activation of water (**relations (5.6 (c), (d))**) [49].

$$\mathrm{CD + H_2O \rightarrow CD - OH + H^+ + e^-} \qquad \textbf{(5.6 (a))}$$

$$\mathrm{CD - OH + Pt_S - CO \rightarrow CD + Pt_S + CO_2 + H^+ + e^-} \qquad \textbf{(5.6 (b))}$$

$$\mathrm{TiO_2 + H_2O \rightarrow TiO_2 - OH + H^+ + e^-} \qquad \textbf{(5.6 (c))}$$

$$\mathrm{TiO_2 - OH + Pt_S - CO \rightarrow TiO_2 + Pt_S + CO_2 + H^+ + e^-} \qquad \textbf{(5.6 (d))}$$

On the other hand, experiments carried out by Sun *et al.* have revealed that the binding energy of CO on the Pt surface is weakened by the presence of oxygen-containing groups on the CD surface [19]. As a result, CO is stripped off from its surface. The effect of oxygen-containing groups in lowering the Pt_S-CO binding energy has also been verified by density functional theory computations by Sharma *et al.*[50]. Linear sweep voltammetry (LSV) experiments were also carried out with the Pt*y*/CD2/TiO_2 catalyst in the same electrochemical environment (**Figure 5.11 (d)**). The LSV plots reveal that the Pt3/CD2/TiO_2 photo-electrocatalyst under simulated solar light exhibits the lowest onset potential of MOR, corroborating the results obtained from the CV measurements.

CDs act as a powerful energy transfer component in the photo-electrocatalytic design due to its up-conversion property. Based on this, the role of CD in the catalytic process has been proposed as illustrated in **Scheme 5.2**. Two types of energy transfer processes occur between CDs and TiO_2 nanoparticles [51]. Firstly, on excitation with visible light, electrons and holes are generated in the CDs. These photo-induced electrons are then injected from the lowest unoccupied molecular orbital (LUMO) level of CDs to the CB of TiO_2 (P1) and contribute to the photocurrent of the system [52]. The second possibility is that photo-generated electrons and holes recombine, and then emit photons of higher energy (up-conversion) (P2). The higher energy photons can then excite TiO_2 for further photo-catalysis of methanol [38].

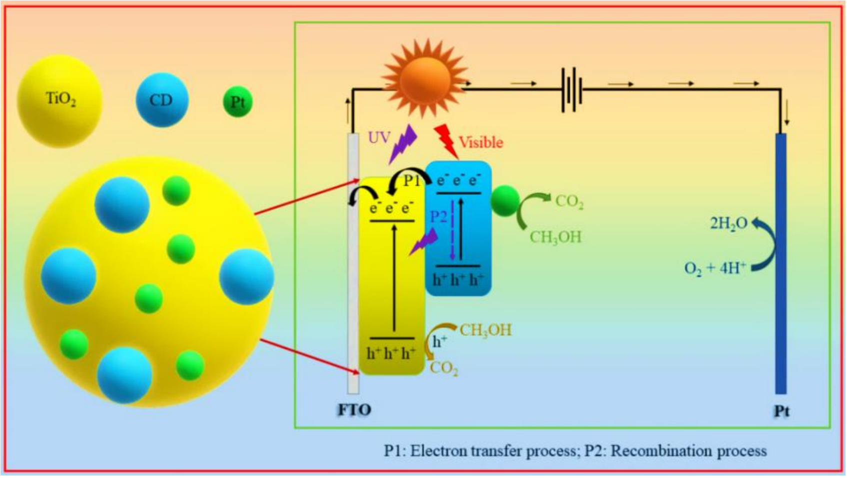

Scheme 5.2 Proposed catalytic mechanism for the electro-photocatalytic oxidation of methanol on CD sensitized TiO_2 supported Pt.

Chronoamperometric technique was applied to study the contribution of photocurrent to the total current density. A fixed potential of 0.6 V was applied and the corresponding chronoamperograms with intermittent illumination for 30 s in repeated off–on cycles were recorded in an electrolyte of 0.5 M CH_3OH and 0.5 M H_2SO_4 as shown in **Figure 5.12 (a)**. Both Pt3/CD2/TiO_2 and Pt3.5/TiO_2 catalysts demonstrate fast as well as consistent transitory photocurrent responses. Initially, the catalysts exhibit a relatively lower current density value in accordance with the CV data. Then with illumination, the current gradually begins to increase, followed by a drop as soon as it is turned off. This is a further confirmation that MOR is greatly enhanced by UV-visible light irradiation through a photo-catalytic process. It is also noteworthy that Pt3/CD2/TiO_2 presents with a better response than Pt3.5/TiO_2, indicating that it possesses a higher efficiency for separation of photo-generated electrons and holes, and their transfer. Furthermore, the composite Pt3/CD2/TiO_2 shows good stability under simulated solar light for upto 100 cycles as shown in **Figure 5.12 (b)**. The decay in current over time is most probably due to the lowering of EASA caused by accumulation of different intermediate species generated during MOR.

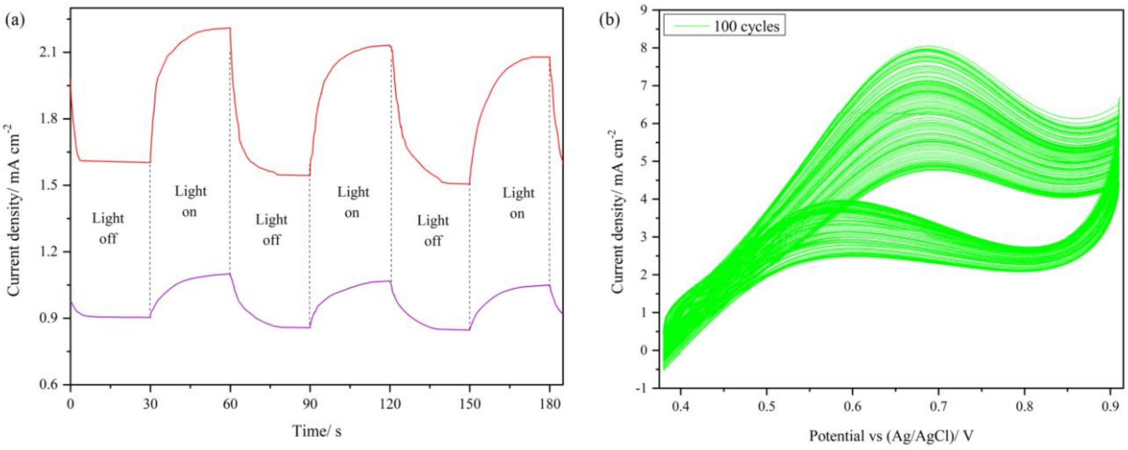

Figure 5.12 (a) Chronoamperometric curves of Pt3/CD2/TiO_2 and Pt3.5/TiO_2 electrodes recorded with intermittent irradiating cycles and **(b)** CV profiles of Pt3/CD2/TiO_2 recorded at 100 mV s^{-1} in the presence of light upto 100 cycles.

Electrochemical impedance spectroscopy (EIS) was employed as an investigative tool to study the changes in electron transport behavior of the electrodes with/ without the addition of CDs in the composite as well as the absence/ presence of simulated solar light irradiation. A 1:1 mixture of 25 mM$K_3[Fe(CN)_6]$/ $K_4[Fe(CN)_6]$ in 0.1 M KCl solution was used as the electrolyte. The data collected in the 0.1 Hz to 100 kHz range were plotted in accordance to the equivalent circuit as shown in the top right inset of **Figure 5.13 (a)**, which includes the series resistance (R_S), the charge transfer resistance (R_{CT}),the Warburg impedance (W) and the double-layer capacitance (C_D). The arc of the semi-circle in the Nyquist plot establishes the R_{CT} value. From **Figure 5.13 (a)**, it can be suggested that the Pt3/CD2/TiO_2 electrode shows better interfacial

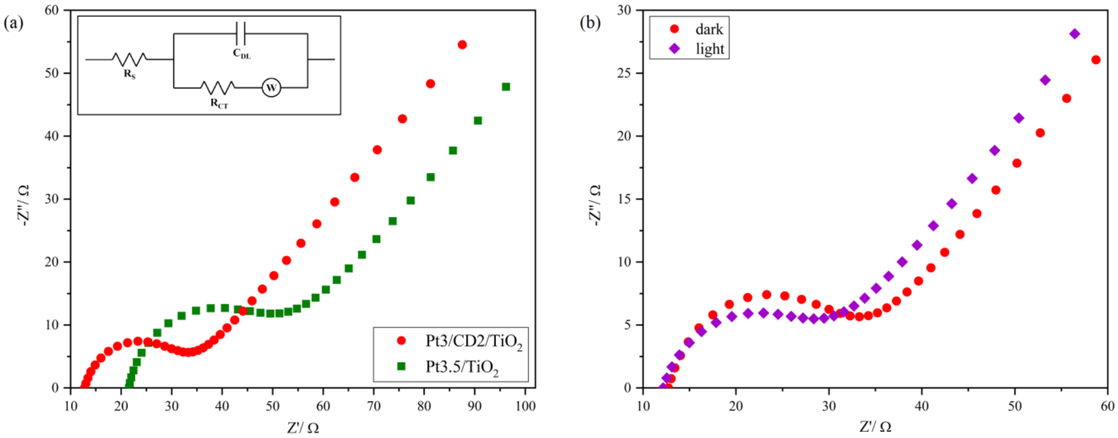

Figure 5.13 (a) EIS curves of Pt3/CD2/TiO_2 and Pt3.5/TiO_2 electrodes recorded in dark (inset: equivalent circuit), and **(b)** EIS curves of Pt3/CD2/TiO_2 under dark and light conditions.

charge transfer than Pt3.5/TiO_2 since the diameter of the arc is noticeably smaller. Considering the diameter of the arc to be a reflection of the rate of the catalytic reaction occurring at the electrode's surface, the smaller arc is also a clear indication of improved electronic conductivity through by the CDs. **Table 5.1** shows the values of R_S and R_{CT} for all the compositions of Pt*y*/CD2/TiO_2 under light and dark conditions. Similarly, enhanced charge transfer can be seen on the photo-illuminated Pt3/CD2/TiO_2 electrode (**Figure 5.13 (b)**), confirming the promotional effect of simulated solar light illumination towards mobility of charges at the electrode's surface.

Table 5.1 EIS parameters of the Pt*y*/CD2/TiO_2 composites under light and dark conditions.

Composite	R_S/ Ω	R_{CT}/ Ω	R_S/ Ω	R_{CT}/ Ω
	Light		Dark	
Pt2.5/CD2/TiO_2	15.06	24.44	15.71	28.13
Pt3/CD2/TiO_2	12.15	17.29	12.73	21.48
Pt3.5/CD2/TiO_2	12.98	19.26	13.48	23.63
Pt4/CD2/TiO_2	13.77	22.01	14.34	25.92

5.5 Conclusion

In conclusion, we have designed a novel CD sensitized TiO_2 supported Pt catalyst for MOR by following a simple route combining hydrothermal method and chemical reduction. A series of catalysts with different wt% of CDs and Pt loading was fabricated, and the catalyst (Pt3/CD2/TiO_2) exhibiting the best performance in terms of catalytic activity, CO poison tolerance and stability was established by means of different electrochemical tests. Owing to the unique up-conversion property of CDs, these catalysts can easily absorb visible light photons from the sunlight and convert them into high energy photons to subsequently excite the TiO_2 nanoparticles. The superior performance of these catalystsis attributed to the two types of catalytic processes occurring simultaneously: photo-catalysis due to CD sensitized TiO_2 and electro-catalysis due to the presence of Pt. This work shows CD in a new light as an inhibitor of CO poisoning as well as a harvester of visible sunlight. The multi-faceted CDs, thus, can provide new possibilities for the rational design of photo-electrocatalysts which can find potential application as anode materials in DMFCs.

Part (b)

Solvothermally Synthesized Green Emitting Carbon Dots as Co-sensitizer in Dye Sensitized Solar Cell

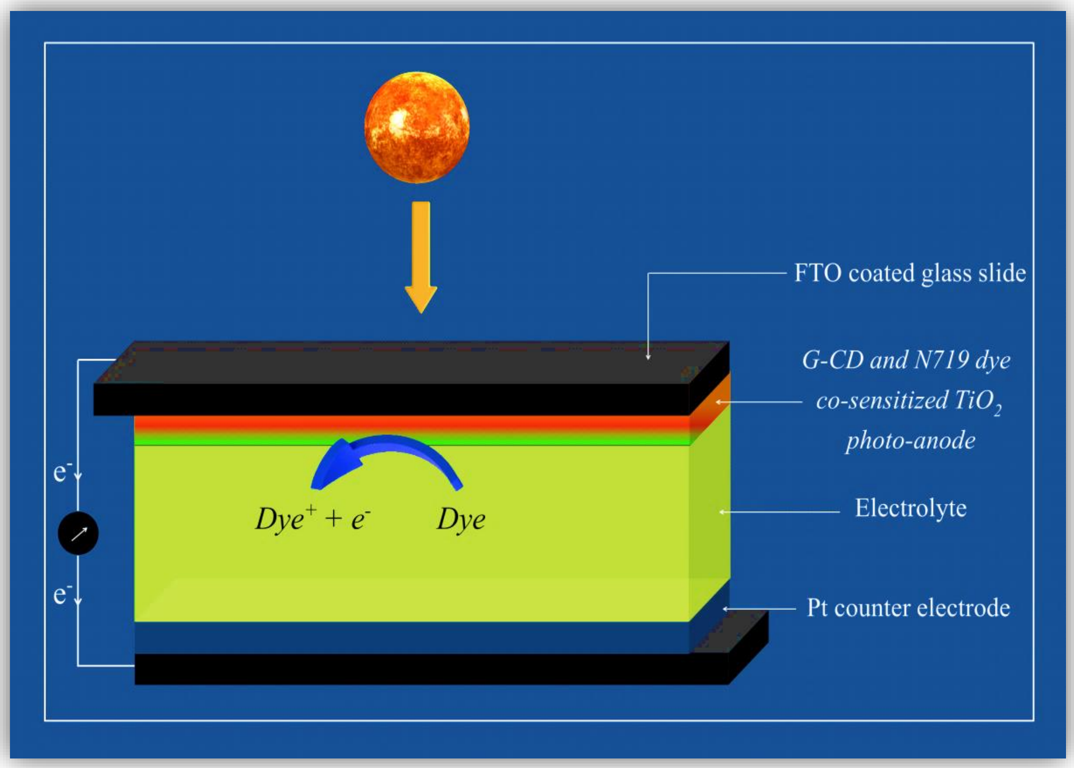

Solvothermal route (in DMF solvent) is used to prepare green emitting carbon dots from citric acid, that are applied as co-sensitizer in DSSC to get improved efficiency by broadening absorption range and energy transfer process.

5.6 Introduction

DSSCs belong to the emerging third generation solar cell technology, which is constructed by sandwiching an electrolyte between a dye sensitized semiconductor anode and a counter electrode [53]. Mesoporous titanium dioxide (TiO_2) is sensitized with dye molecules to act as the photoanode [54]. The ruthenium based dye, N719, is commonly used in DSSCs. It has a single absorption peak lying in the green region of the visible solar spectrum [55]. Due to this, DSSCs suffer from a narrow visible spectral absorption response. However, additional unexploited light can be utilized to widen the absorption region by using different fluorophores and fluorescent materials [56,57].

In the recent times, use of carbon dots (CDs) and its analogues are gaining momentum due to their extraordinary optoelectronic properties. For instance, Tang *et al.* prepared a DSSC with a TiO_2 photoanode sensitized with CDs and covered with green emitting long-persistence phosphor (LPP) [58]. Due to the weak affinity between TiO_2 and CDs, the obtained photoconversion efficiency under illumination was quite low. Working on a similar principle, Zhao *et al.* co-sensitized the TiO_2/green emitting LPP anode with both N719 dye and nitrogen-doped CDs [59]. The hole extraction behavior of nitrogen doped CDs helped in realizing a maximum efficiency of 9.29% under illumination. In our previous work, green emitting CDs were incorporated in the electrolyte of the DSSCs [60]. The emission range of the CDs coincided with the absorption range of the dye molecules, which resulted in significant increase in the efficiency of the DSSC. Following these works, fabricating a device with both N719 dye and green emitting CDs with high N content co-sensitized photoanode presents a good approach for obtaining high efficiency DSSC.

5.7 Materials and methods

5.7.1 Chemicals

Fluorescein, tetrabutylammonium hexafluorophosphate and DMF were purchased from Merck. The chemicals used for preparing CDs and fabricating the solar cell are mentioned

---

This part of the thesis is communicated as:

Bora, A., Mohan, K., and Dolui, S. K. Enhancing the efficiency of dye sensitized solar cell by employing green emitting carbon dots as co-sensitizers. (*Communicated*) elsewhere. Distilled water was used for all purposes.

5.7.2 Synthesis of CDs

For preparing green emitting CDs, the synthesis process mentioned in *Part (a)* was slightly modified. A solution of 0.6 g of citric acid in 20 mL DMF was prepared. Then 0.17 mL of ethylenediamine was added to it. The solution was then transferred to a Teflon lined autoclave and heated at 180 °C for 5 h. After completion of the reaction, green emitting CDs were obtained.

5.7.3 Fabrication of DSSC

The procedure used for fabricating the solar cell is mentioned in *Section 3.2.3 of Chapter 3*. However, the photo-anode fabrication step was slightly modified towards the end. Once the TiO_2 coated substrate has been dipped in N719 dye solution for 24 h and dried to obtain N719 dye sensitized TiO_2 anode, an additional step is followed. For co-sensitizing it with CDs, a 2 mg mL^{-1} dispersion of CDs in acetonitrile was spin coated onto the dye sensitized TiO_2 electrode. The electrode was heated at 50 °C for 12 h. Finally, the CD and N719 dye co-sensitized TiO_2 electrode was used as the photo-anode. For comparison purposes, TiO_2 photoanode sensitized with only N719 dye was also prepared.

5.7.4 Characterization

The instruments used for characterizing the CDs, and obtaining the current density-voltage (J-V) characteristics of the DSSCs are described in *Part (a)* and *Section 3.2.4 of Chapter 3*. The fill factors (FF) and photoconversion efficiencies (η) of the devices were calculated from the J-V plots using **relations (3.1)** and **(3.2)** mentioned in *Chapter 3*. All other electrochemical measurements were performed on a Bio-Logic SP-150 potentiostat.

5.7.5 Quantum yield measurement

Five different concentrations each of CDs and fluorescein were prepared in distilled water (η = 1.33) and 0.1 M NaOH (η = 1.33) respectively. The UV-visible absorbance intensities and the PL intensities of all the samples were recorded at their excitation wavelengths (490 nm). The literature value of the quantum yield of fluorescein ($\Phi_{Fluorescein}$) is 0.95. The integrated PL intensities of each sample at different concentrations were plotted against their corresponding absorbance values. From the slopes of the plotted lines (s), the quantum yield of CDs (Φ_{CD}) was calculated by using **relation (5.7)** [61].

$$\Phi_{CD} = \Phi_{Fluorescein}(s_{CD} / s_{Fluorescein})(\eta_{water}^2 / \eta_{0.1\ M\ NaOH}^2) \tag{5.7}$$

5.8 Results and discussion

In this study, solvothermal route was selected to prepare green emitting CDs using DMF as the reaction medium with citric acid as the carbon source.

5.8.1 Characterization of CDs. In our study, solvothermal route was selected to prepare CDs using DMF as the reaction medium with citric acid as the starting material. The CD nanoparticles show a characteristic broad peak around 3411 cm^{-1} due to O–H/N–H stretching vibrations in their FTIR spectrum (**Figure 5.14 (a)**). The peak at 2937 cm^{-1} belong to asymmetric while a slight hump adjacent to it at 2868 cm^{-1} is due to symmetric C–H stretching vibration. Three other peaks around 1698 cm^{-1}, 1657 cm^{-1} and 1403 cm^{-1} are also observed, which can be ascribed to C=O/C=N, C=C and–CN stretching vibrations respectively. XPS measurements of the CDs were carried out to determine their chemical composition. The full-scan XPS spectrum, presented in **Figure 5.14 (b)**, shows that the CDs are made up of the elements C, N and O. The peak of C1s appears at 284.2 eV, that of N1s appears at 398.3 eV, while the peak at 531.9 eV belongs to O1s [62]. The atomic percentages, as obtained from XPS analysis, show that the CDs contain 73% C, 9% N and 18% O. A uniform distribution of these three elements is also seen in the EDX elemental mapping images of CDs (**Figure 5.14 (c-f)**).

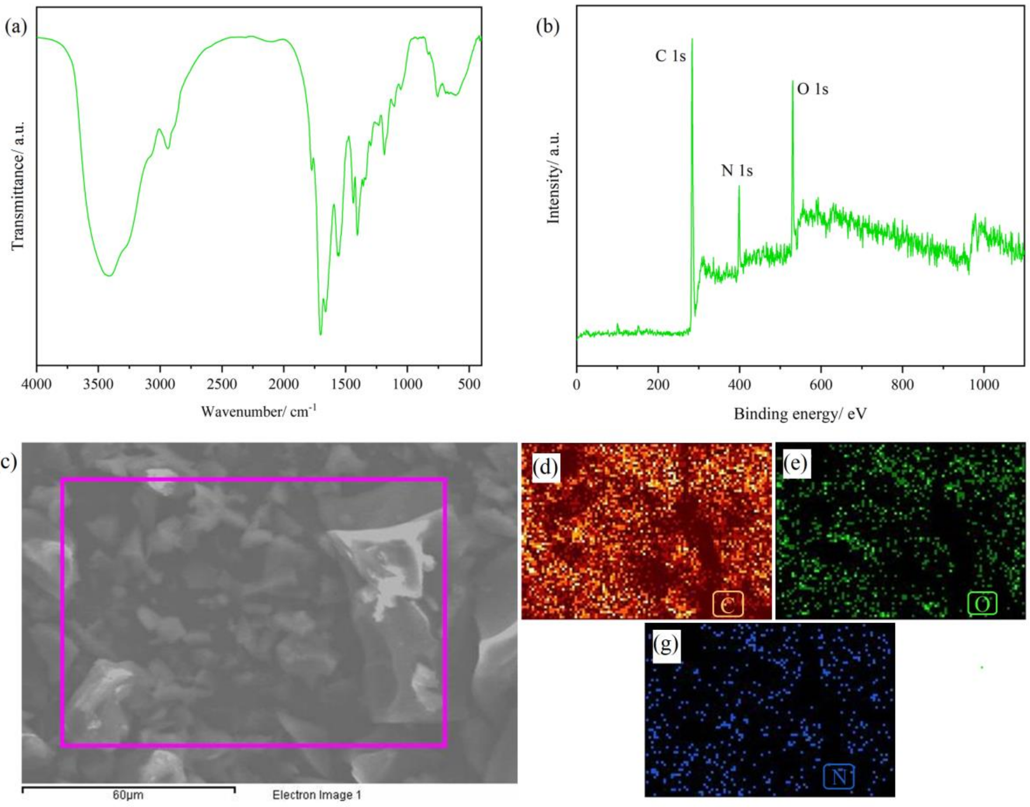

Figure 5.14(a) FTIR spectrum, **(b)** XPS spectrum and **(c-f)** EDX elemental mapping images of CDs.

The TEM image of CDs is shown in **Figure 5.15 (a)**.The nanoparticles show good dispersion and are mostly spherical in shape. Majority of the particles possess poor crystallinity, and their DLS histogram shows a narrow size distribution in the range 4-8 nm (**Figure 5.15 (b)**). However, the HRTEM image reveals a few particles with 0.21 nm lattice spacing. This corresponds to (100) lattice plane of graphene [63]. The XRD pattern of the particles also shows the existence of this plane in addition to (002) plane at around 2θ = 23° (**Figure 5.15 (c)**).

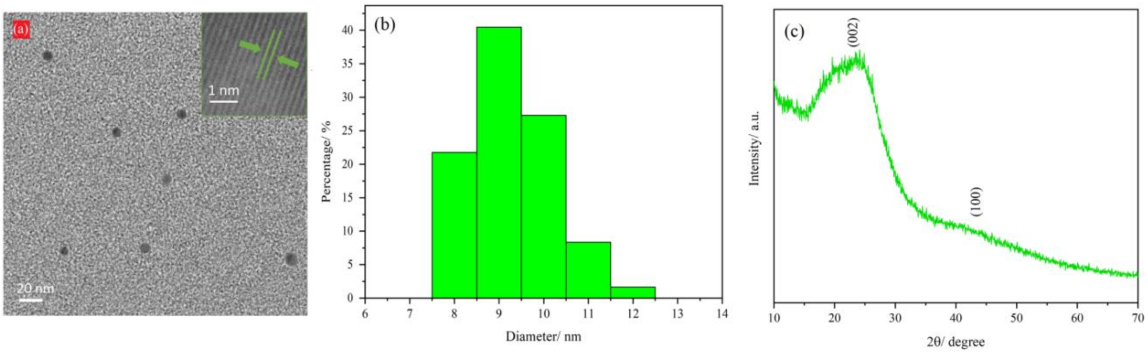

Figure 5.15 (a) TEM micrograph, **(b)** DLS number distribution and **(c)** XRD pattern of CDs.The inset of **(a)** shows the HRTEM image of CDs.

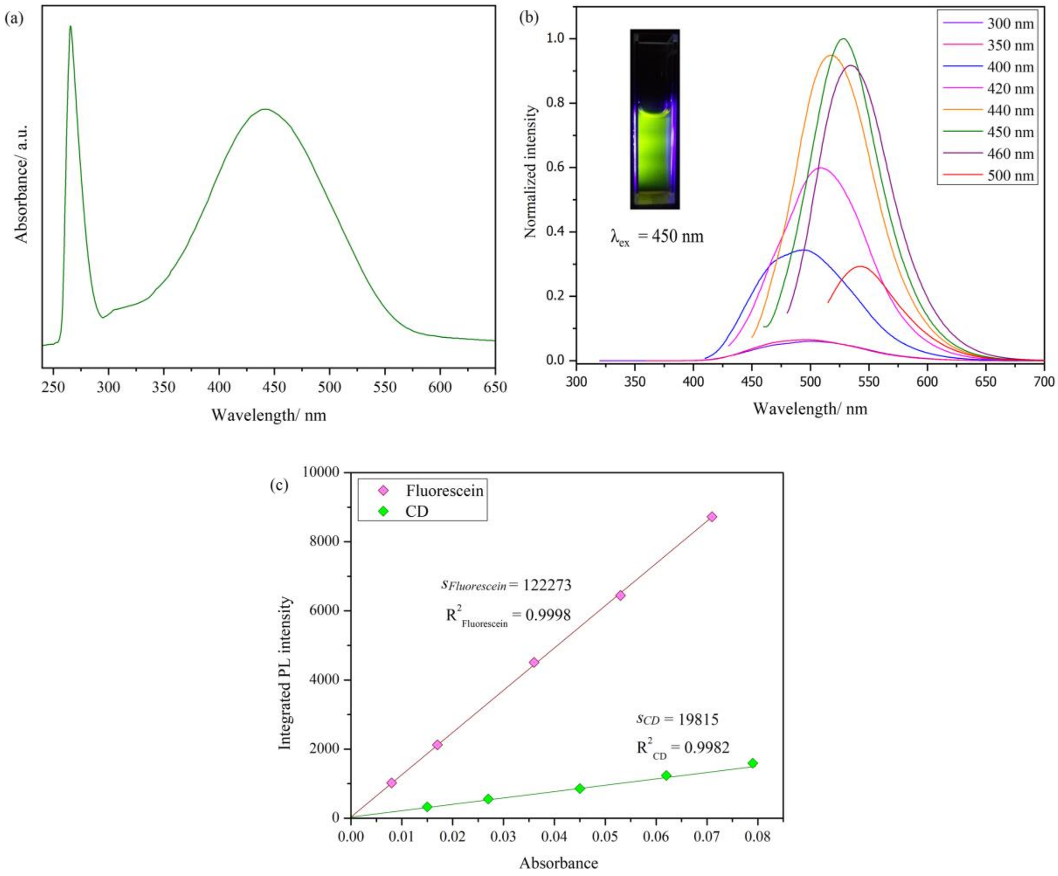

Figure 5.16 (a) UV-visible absorption and **(b)** PLemission spectra of CDs.The inset of **(b)** shows the digital image of the CDs. **(c)** PL *vs.* absorbance plots of CDs and fluorescein.

The UV-vis spectrum of the CDs is shown in **Figure 5.16 (a)**. A sharp peak appears at 265 nm due to π–π* transition within the aromatic C core. This peak does not generate any fluorescence signal in CDs. The origin of fluorescence in CDs is largely attributed to the second, lower-energy transition, which appears at 442 nm. At longer wavelengths, the eventuality of n–π* transitions becomes increasingly less. So, this absorption peak can be attributed to the presence of surface states [64], which results in the emission of green colored fluorescence with a maximum emission PL peak at 528 nm (**Figure 5.16 (b)**). The quantum yield of CDs was calculated with reference to fluorescein standard, and was found to be 15.4% at the excitation wavelength of 490 nm (**Figure 5.16 (c)**).

5.8.2 Performance of G-CD and N719 dye co-sensitized solar cell. The effect of co-sensitization of N719 sensitized DSSC with CDs was assessed using the *J-V* characteristics of the device under irradiation of light (AM 1.5G). The results are presented in **Figure 5.17** and the photovoltaic parameters are listed in **Table 5.2**. The co-sensitized device achieved a conversion efficiency of 6.9% through a high J_{SC} value of 14.23 mA cm^{-2} and V_{OC} value of 0.763 V. In comparison, the efficiency of N719 dye sensitized cell is slightly lower at 6.28%, thus the favorable effect CDs as co-sensitizer is justified.

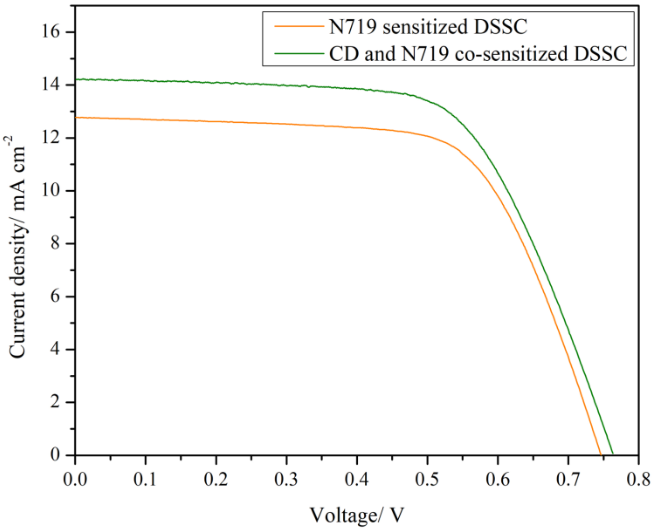

Figure 5.17 *J-V* characteristic plots of N719 sensitized, and CD and N719 co-sensitized DSSC.

Table 5.2 Photovoltaic parameters of N719 sensitized, and CD and N719 co-sensitized DSSC.

Sensitizer	J_{SC}/ mA cm^{-2}	V_{OC}/ V	*FF*	η/ %
N719 dye	12.78	0.746	0.66	6.28
CD and N719 dye	14.23	0.763	0.63	6.90

The performance of a DSSC relies to a huge extent on the sunlight absorption capacity of the sensitizers, as well as the transfer of photo-excited electrons from the sensitizers through the TiO_2 film to the outer circuit. The N719 dye usually absorbs sunlight at 533 nm (**Figure 5.18)**, which excites the electrons from the highest occupied molecular orbital (HOMO) to the lowest unoccupied molecular orbital (LUMO) level. Generally, these photo-excited electrons from the LUMO level of the dye then transfer to the conduction band (CB) of TiO_2, and then onto the outer circuit. The photo-generated holes from the HOMO level of N719 dye, on the other hand, promote the oxidation of iodide (I^-) ions in the electrolyte.

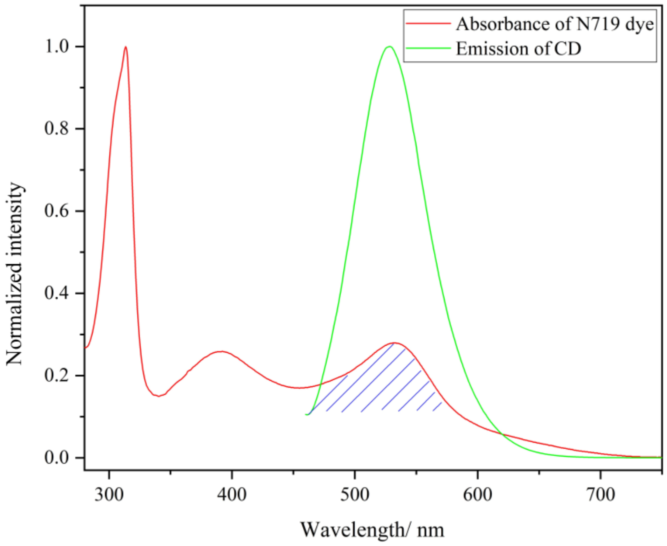

Figure 5.18 UV-visible spectrum of N719 dye, and overlap of the CD emission spectrum with N719 dye absorption spectrum.

In order to elucidate the role of CDs in the DSSC, their HOMO and LUMO levels were calculated from their cyclic voltammogram **(Figure 5.19)**[65,66]. A three-electrode set-up was used to record the CV profiles, with a glassy carbon electrode working electrode, an Ag/AgCl reference electrode and a platinum wire counter electrode. The electrolyte consisted of a solution containing 0.1 M tetrabutylammonium hexafluorophosphate as the supporting electrolyte in acetonitrile with 0.1 mg mL^{-1} CDs. The scan rate was maintained at 25 mV s^{-1}. The HOMO and LUMO energy levels were determined using **relations(5.8 (a))** and **(b)**:

$$E_{HOMO} = -(E_{onset,ox} + 4.4)eV \qquad \textbf{(5.8 (a))}$$

$$E_{LUMO} = -(E_{onset,red} + 4.4)eV \qquad \textbf{(5.8 (b))}$$

whereE_{HOMO} and E_{LUMO} are the HOMO and LUMO energy levels respectively. $E_{onset,ox}$ and $E_{onset,red}$ are the onset oxidation and reduction potentials. The HOMO and LUMO levels of CDs were found to be -5.3 eV and -3.1 eV respectively.

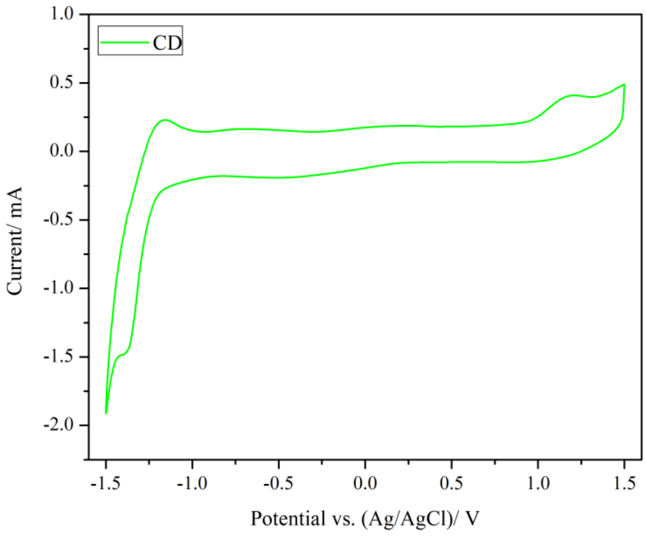

Figure 5.19 CV profile of CDs recorded at a scan rate of 25 mV s^{-1}.

Now, the role of CDs can be considered to be three-fold. First, it can improve the charge extraction process in the photoanode *via* a route denoted by **P1** in **Scheme 5.3**, in which the CDs can additionally absorb sunlight at 442 nm, and contribute to the electron density at the LUMO level of N719 dye. The more positive LUMO energy level of CDs in comparison to that of N719 dye (-3.9 eV) facilitates this electron transfer process. The photo-generated holes from the HOMO level of N719 dye (-5.4 eV) can also contribute to the hole density in the HOMO level of CDs and help in the oxidation of I^- ions. Ultimately, better alignment of the energy levels of each component contributes to a better charge extraction process. There is also a second possibility of emission of light by the CDs in the green spectrum (528 nm), denoted by process **P2**, which coincides with the absorption range of N719 dye. This can cause further excitation of the N719 dye molecules and increase the number of charges at the photoanode. Both the process, **P1** and **P2**, eventually leads to an increase in the magnitude of J_{SC} of the co-sensitized solar cell. In a third probable situation, the CDs can act as an additional layer between the photo-excited electrons in the CB of TiO_2 and the electrolyte, and suppress the dark reaction of triiodide ion (I_3^-) reduction at the surface of TiO_2 [59].

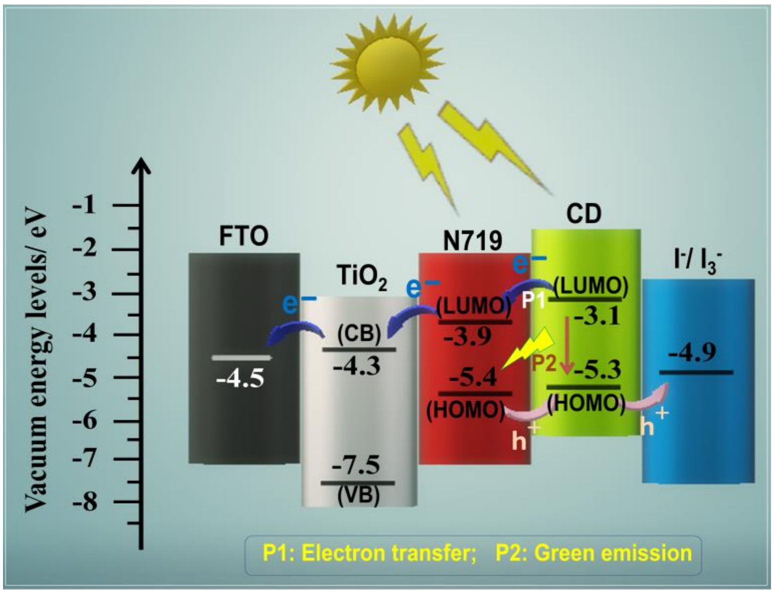

Scheme 5.3 Energy level diagram showing the favorable influence of CDs as co-sensitizer in the photoanode.

The *J-V* characteristic plot of the co-sensitized cell also indicates an enhancement in the value of V_{OC}. Mathematically, V_{OC} can be expressed in terms of the difference between the Fermi level of the photoanode (E_F) under illumination and the redox potential of the electrolyte (E_{redox}) (**Relation (5.9 (a))**).

$$V_{OC} = \frac{E_F - E_{redox}}{q} \qquad \textbf{(5.9 (a))}$$

where$q$ is the charge.

$$E_F = E_C + kTln\frac{n_C}{N_C} \qquad \textbf{(5.9 (b))}$$

Relation (5.9 (b)) represents E_F where E_C is the TiO_2 CB edge, and n_C and N_C are the free electron density and density of accessible states in the CB of TiO_2. Thus, V_{OC}can ultimately be represented as **relation (5.9 (c))**.

$$V_{OC} = \frac{kT}{q}\left(\frac{E_C - E_{redox}}{kT} + ln\frac{n_C}{N_C}\right) \qquad \textbf{(5.9 (c))}$$

It follows from **relation (5.9 (c))** that a higher value of n_C can increase the magnitude of V_{OC}. In case of the co-sensitized device, photo-excited electrons from CDs add to the electron density at the CB of TiO_2 and enhance the value of V_{OC}from0.746 Vto 0.763 V.

In order to gain insight into the electron transport processes at the electrode/electrolyte interfaces of the DSSCs, their EIS spectra were recorded at a bias of 0.75 V. **Figure 5.20** shows the Nyquist plots (*Z'* vs –*Z''*) fitted with an equivalent circuit as shown in the inset. Each plot comprises three semicircles representing different types of electron transport resistances [67]. The intercept on the *x* axis represents the series resistance, $R_S$of the cell. This value is almost same for both the types of DSSCs as tabulated in **Table 5.3**. The first semicircle in the high frequency region corresponds to charge transfer resistance at the Pt counter electrode/electrolyte interface ($R_{CT,CE}$), while the second semicircle in the mid frequency region occurs due to charge transfer resistance at the photoanode/electrolyte interface ($R_{CT,PA}$) and is our region of interest. The last semicircle in the low frequency region is due to Warburg diffusion process of the iodide/triiodide ions in the electrolyte (*W*). A comparison of the $R_{CT,PA}$values (from the radius of the middle semicircle) indicates a decrease when CDs are used as co-sensitizers. So it can be concluded that presence of CDs increases rate of electron transfer rate at the interface, which is most likely due to the improved charge extraction capacity of the photoanode.

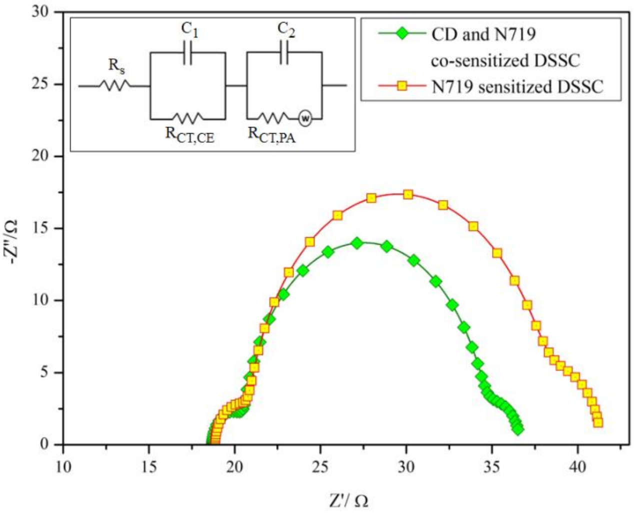

Figure 5.20 Nyquist plots of N719 sensitized DSSC, and CD and N719 co-sensitized DSSC. The inset shows the equivalent circuit.

Table 5.3 EIS parameters of N719 sensitized DSSC, and CD and N719 co-sensitized DSSC.

Sensitizer	R_S/ Ω	$R_{CT,CE}$/ Ω	$R_{CT,PA}$/ Ω
N719 dye	18.86	1.98	16.95
CD and N719 dye	18.72	1.83	13.78

Finally, the efficiency of our device is compared with a few other reported CD sensitized DSSCs and presented in **Table 5.4**. They fare favorably when compared to DSSCs that have only CD sensitized TiO_2 photoanode. This is mostly due to weak bonding between CD molecules and TiO_2 nanoparticles. But in cases where both LPP and N719 dye is used, they show comparable results.

Table 5.4 Summary of performances of different CD sensitized DSSCs under illumination.

Photoanode	J_{SC}/ mA cm^{-2}	V_{OC}/ V	FF	η/ %	Ref.
CD/TiO_2	0.53	0.38	0.64	0.13	[2]
N doped CD/TiO_2	0.69	0.46	0.43	0.13	[68]
CD/TiO_2 nanotubes	0.02	0.58	0.35	0.0041	[69]
CD/ZnO nanotubes	0.67	0.26	0.43	0.077	[70]
RhB/CD/TiO_2	~0.69	~0.5	-	0.147	[71]
LPP/CD/TiO_2	0.491	0.667	0.52	0.17	[58]
LPP/N doped CD/N719/TiO_2	18.6	0.736	0.68	9.29	[59]
Present work (CD/N719/TiO_2)	14.23	0.763	0.63	6.90	-

5.9 Conclusion

In conclusion, we have synthesized CDs using solvothermal route from citric acid using DMF as the reaction medium. XPS result shows that these CDs contain a significant amount of N, resulting in green colored emission. Coincidently, the emission spectrum of CDs overlaps with the absorption spectrum of the N719 dye used in DSSCs, giving rise to the possibility of energy transfer occurring between them, along with the utilization of additional blue spectral region by the CDs. Moreover, favorable band alignment of all the components of the DSSC results in an improved photoconversion efficiency (6.9%) when the solar cell is co-sensitized with CDs. Overall, we have developed a simple approach for obtaining high efficiency DSSC using green emitting CDs as co-sensitizer along with the conventional N719 dye.

Part (c)

Solvothermally Synthesized Blue Emitting Carbon Dots as Fluorescence Sensor for 2,4,6-Trinitrophenol Detection in Organic Medium

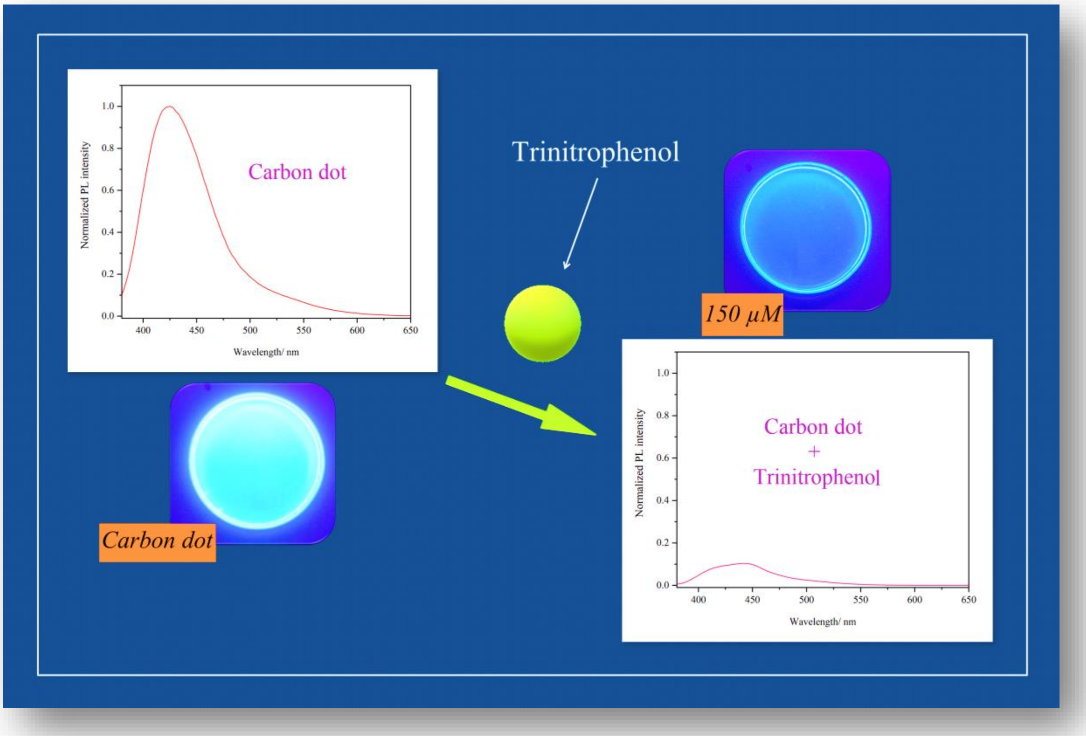

Solvothermal route (in DMF solvent) is used to prepare blue emitting carbon dots from gallic acid, and these are used as the sensing element for a fluorescence based platform for detection of 2,4,6-trinitophenol in DMF medium.

5.10 Introduction

TNP, popularly known as picric acid, is a strong organic acid that is an integral part of chemical laboratories as well as many industries including dye, leather and pharmaceuticals. Despite its importance, it cannot be denied that TNP is an explosive and a bio-toxic nitroaromatic compound (NAC) that can cause strong irritation to skin, eyes and respiratory systems on overexposure [72]. In addition to being detrimental to the environment (poorly biodegradable) and human health (mutagenic property), its determination is also crucial for national security against terrorist threat. Photoluminescence (PL) quenching based method is especially popular because of its quick response time, simplicity and inexpensiveness [32]. The reported PL based detection platforms comprise fluorescent materials whose fluorescence intensity is quenched in the vicinity of the analyte. For instance, Nagarkar*et al.* reported a luminescent 3D porous metal-organic framework, $[Cd(NDC)_{0.5}(PCA)]\cdot G_x$(where NDC = 2,6-napthalenedicarboxylicacid, PCA = 4-pyridinecaboxylic acid and G = guest molecules) that could selectively detect TNP upto 4 µM [75]. Na *et al.* presented a system using lysozyme-capped CdS quantum dots to detect TNP with a detection limit of 0.1 µM [76]. Although very effective, one cannot deny the toxic nature of the heavy metals present in metal organic frameworks and quantum dots.

As an environmental friendly and non-toxic alternative, CDs have emerged as significant fluorescence sensing element in the recent years due to their high sensitivity. Wang *et al.* were the first to explore the non-selective fluorescence quenching behavior of CDs in the presence of NACs *viz.* 4-nitrotoluene and 2,4-dinitrotoluene in toluene solution [77]. Following their work, Niu*et al.* synthesized amine-capped CDs and applied them as sensor for detection of TNP with a detection limit of 1 µM[78]. Since then, other researchers have also reported similar works with the aim to achieve improved sensitivity and selectivity with a large detection range. Such works include preparation of orange emissive CDs by Ren *et al.* which were rapidly and selectively quenched by TNP with a detection limit of 0.127 mM[79]. Shi et al. used CDs prepared from sucrose phosphate solution for sensing TNP with a limit of detection of 16.9 nM which was based on the phenomenon of fluorescence resonance energy transfer (FRET) [80].

This part of the thesis is communicated as:

Bora, A., Mohan, K., and Dolui, S. K. Gallic acid derived hydrophobic carbon dots as fluorescence sensor for 2,4,6-trinitrophenol detection in organic medium. (*Communicated*)

Although water is the most common medium for TNP pollution, the importance of common organic media like tetrahydrofuran (THF) and *N*,*N*-dimethylformamide (DMF) as carriers cannot be discounted. An extensive literature review revealed only one report where hydrophobic CDs, synthesized by a green method, were used for determination of TNP in the organic solvent THF [81]. Hydro(solvo)thermal route is fairly popular for obtaining high quantum yield CDs from green precursors like citric acid. But the CDs thus produced are mostly water soluble. This necessitates the expansion of the search for the source of carbon to include those that can ultimately produce CDs soluble in aprotic/organic solvents so as to achieve our objective of designing a platform for detecting TNP in DMF medium. Previously, pyrogallic acid has been used to produce green emitting CDs by Du *et al.*[82]. Joseph *et al.* used tannin acid, which has ten gallic acid units attached to a glucose core, to prepare CDs [83]. Since gallic acid is electron-rich, it rendered the CDs with electron-rich surface functional groups during the synthesis process. TNP, on the other hand, is electron-withdrawing, so it led to the formation of a complex between the two resulting in fluorescence quenching. In the third part of this chapter, blue emitting CDs are prepared from gallic acid that are soluble in DMF, and are able to detect TNP molecules in the organic medium.

5.11 Materials and methods

5.11.1 Chemicals

All the materials required to prepare CDs, and TNP, p-nitrophenol (p-NP) and 2,4-dinitriphenol (2,4-DNP) were purchased from Merck.

5.11.2 Synthesis of CDs

For preparing CDs, citric acid in the previous part (*Part (b)*) was replaced with 0.6 g gallic acid and 0.17 mL ethylenediamine was used to carry out the reaction in DMF medium. After completion of the solvothermal reaction, blue emitting CDs were obtained.

5.11.3 TNP sensing protocol

In order to study how TNP affects the fluorescence intensity of CDs, a simple protocol was established in which 10 mL of the 0.01 mg mL^{-1} CDs solution in DMF was regarded as the standard, and all emission intensities measured thereafter were compared with PL spectrum of this solution at excitation wavelength of 365 nm. Next, calculated quantities of TNP (in the range of 1-250 µM) were added to the CD solution, and kept at room temperature for an appropriate period of incubation time. The PL spectra of solutions were measured at the end of the incubation period (10 min).

5.11.4 Characterization

The instruments used for characterizing CDs are mentioned in *Part (a)*.

5.11.5 Quantum yield measurement

Five different concentrations each of CDs and fluorescein were prepared in DMF (η = 1.43) and 0.1 M H_2SO_4 (η = 1.33). The UV-visible absorbance intensities and the PL intensities of all the samples were recorded at their excitation wavelengths (340 nm). The literature value of the quantum yield of QS (Φ_{QS}) is 0.54. The integrated PL intensities of each sample at different concentrations were plotted against their corresponding absorbance values. From the slopes of the plotted lines (s), the quantum yields of CDs $(\Phi)_{CD}$ was calculated by using **relation (5.10)**.

$$\Phi_{CD} = \Phi_{QS}(s_{CD} \,/\, s_{QS})(\eta^2_{DMF} \,/\, \eta^2_{0.1\ M\ H_2SO_4}) \qquad \textbf{(5.10)}$$

5.12 Results and discussion

In this study, solvothermal route was selected to prepare hydrophobic blue emitting CDs using DMF as the reaction medium with gallic acid as the carbon source.

5.12.1 Structural and elemental analyses. The FTIR spectrum of solvothermally synthesized hydrophobic CDs derived from gallic acid is shown in **Figure 5.21 (a)**. The CDs exhibit a large broad peak centered around 3399 cm^{-1} due to O–H/N–H and another at 1663 cm^{-1} due C=O stretching vibrations. The existence of both theses peaks signifies the presence of –COOH functional group. The characteristic peaks of asymmetric and symmetric C–H stretching vibrations occur at 2931 and 2860 cm^{-1}. Another peak centered at 1624 cm^{-1} is also observed, which can be ascribed to C=C stretching. The intensity and type of the functional groups present in CDs plays an integral role in their solubility in different types of solvents [84]. The availability of lesser number of oxygen containing functional groups in CDs imparts the nanoparticles with a hydrophobic character. However, they can easily disperse in organic solvents like DMF.

The elemental composition of the CDs as given by their XPS spectrum (**Figure 5.21 (b)**) shows the presence of the elements C, N and O with the peaks at 284.2 eV, 398.3 eV and 531.9 eV belonging to the binding energies of C1s, N1s and O1s respectively. The EDX elemental mapping images show a uniform distribution of these three elements with the density gradually decreasing from C to O to N (**Figure 5.21 (c-f)**).

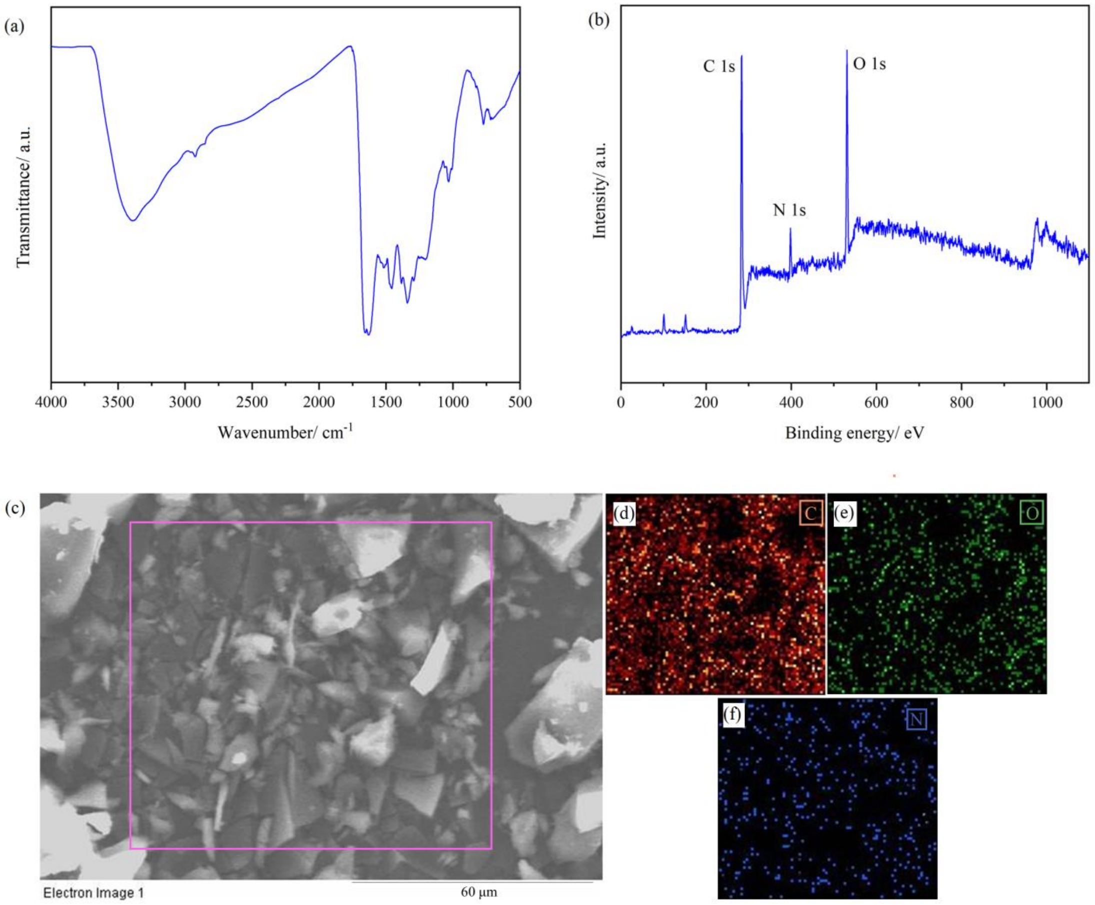

Figure 5.21(a) FTIR spectrum, **(b)** XPS spectrum and **(c-f)** EDX elemental mapping images of CDs.

CDs are mostly spherical with good dispersion in their TEM micrograph (**Figure 5.22 (a)**). The particles are predominantly amorphous and show a narrow size distribution ranging

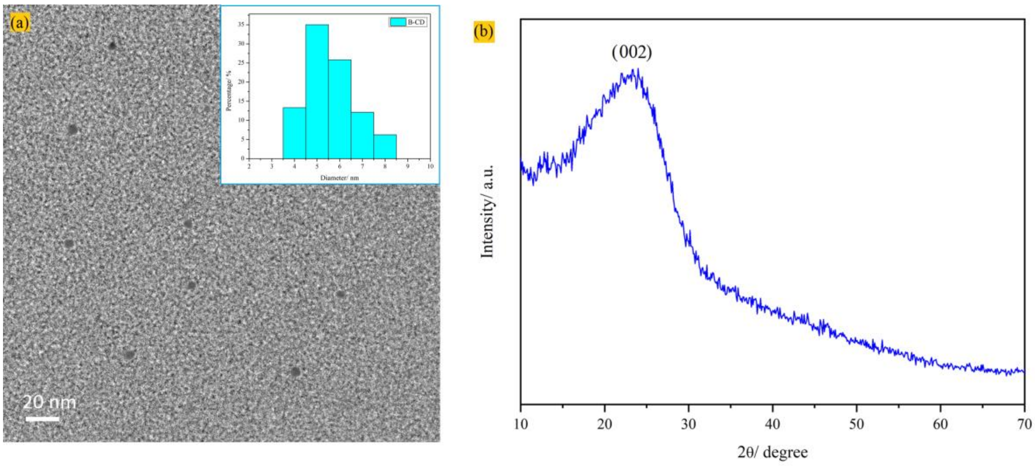

Figure 5.22 (a) TEM micrograph and **(b)** XRD pattern of CDs.The inset of **(a)** shows the corresponding DLS number distribution.

between 4-8 nm as obtained from DLS number measurement (**Figure 5.22 (a, inset)**). The XRD pattern of CDs shows the existence of a broad peak centered at 2θ = 23° that belongs to the (002) plane of graphite (**Figure 5.22 (b)**). In general, for graphite with an ordered crystal structure, this peak (sharp) appears at 2θ = 26.5°, but in our case a downward shift is seen associated with broadening of the peak. This observation can be attributed to the presence of highly disordered carbon as well as a change in the sp^2 C structure during the CD formation process [85].

The CDs show two distinctive UV-visible peaks (**Figure 5.23 (a)**). The lower wavelength peak at 269 nm is ascribed to π–π^* transition within the carbonic/aromatic core (C=C). In accordance with previous reports, n–π^* transition of C=O bond of functional groups leads to another UV-visible peak at 283 nm. Consequently, a blue colored emission is obtained centered at 424 nm when they are excited at 365 nm (**Figure 5.23 (b)**), with a quantum yield of 25.4% **(Figure 5.23 (c)**).

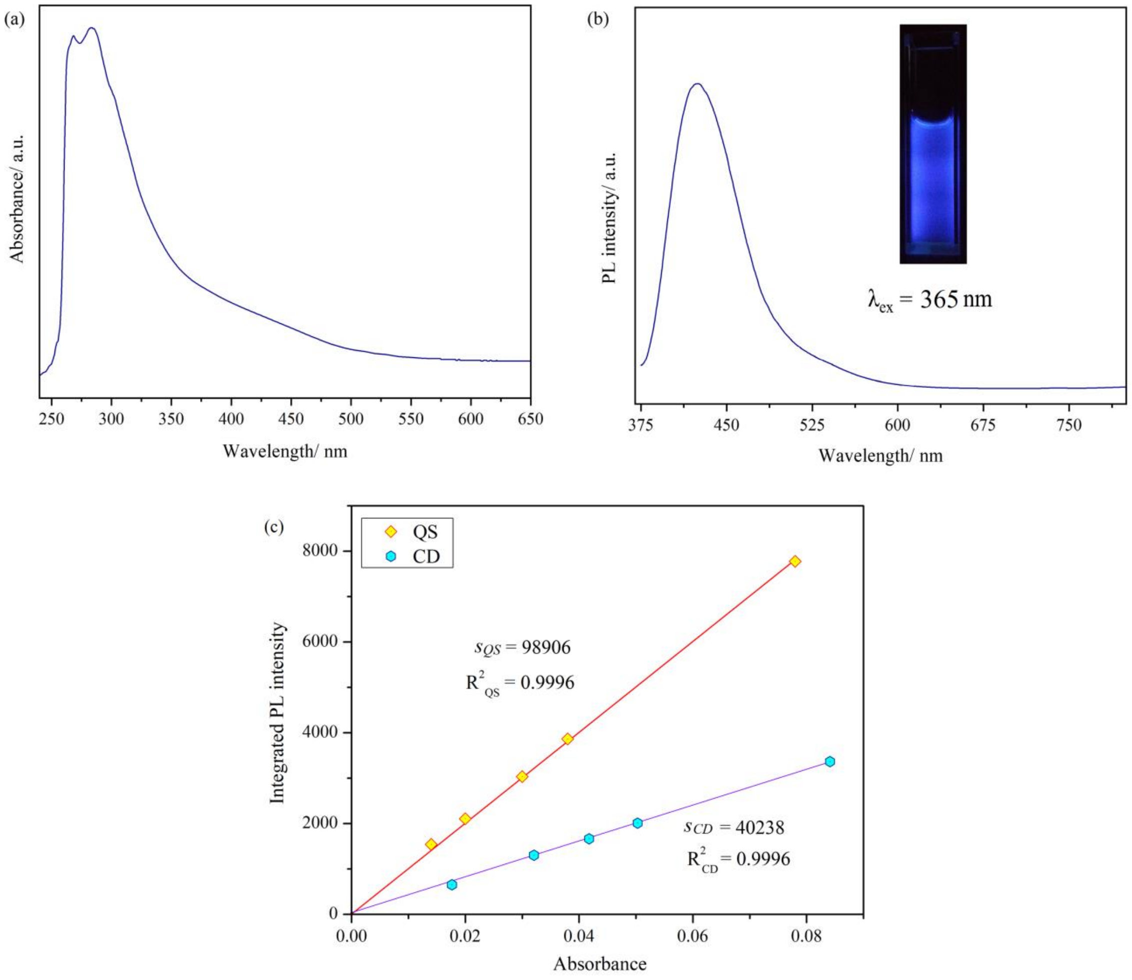

Figure 5.23 (a) UV-visible absorption and **(b)** PLemission spectra of CDs.The inset of **(b)** shows the digital image of the CDs. **(c)** PL *vs.* absorbance plots of CDs and QS.

5.12.2 Detection of TNP using CDs.A fluorescence quenching experiment was designed with different concentrations of TNP to explore the feasibility of using CDs for their detection. In the absence of TNP, the PL spectrum of CDs dispersed in DMF exhibits a strong emission peak at 426 nm when excited at 365 nm. However, the PL intensity of CDs is gradually quenched with the addition of TNP solutions (**Figure 5.24 (a)**).

To analyze the quenching behavior, the Stern-Volmer equation was applied (**relation (5.11)**).

$$\frac{I_o}{I} - 1 = K_{SV}[C] \tag{5.11}$$

where I_o and I are the PL intensity before and after addition of the analyte, K_{SV} is the Stern-Volmer quenching constant, and [C] is the molar concentration of the analyte. K_{SV} represents the quenching efficiency. The relative PL intensities were plotted against different concentrations of TNP (Stern-Volmer plot), and K_{SV}value of 2.6 x 10^4 M^{-1} was obtained from the linear part of the plot (0-100 µM) with a limit of detection (LOD) of 0.75 µM (**Figure 5.24 (b)**). It is noteworthy that the Stern-Volmer plot displays an exponential increase at higher concentrations of TNP (> 100 µM).

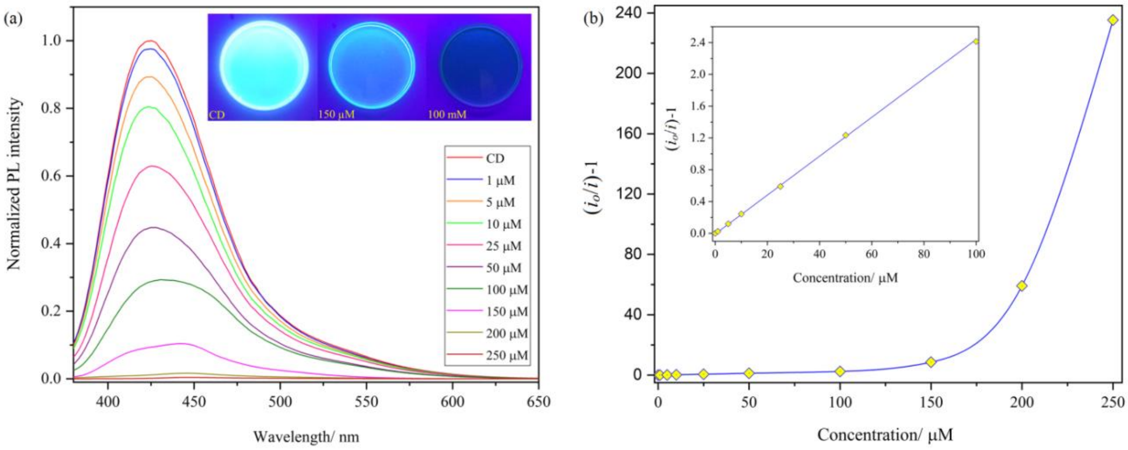

Figure 5.24 (a) Variation of PL emission of CDs with addition of TNP of different concentrations (the inset shows the digital photographs of quenching of blue emission of CDs with addition of TNP at λ_{ex} = 365 nm) and **(b)** Stern-Volmer plot for TNP sensing at different concentrations (the inset shows the linear range from 0-100 µM).

For any material to be an effective sensing element, it is of utmost importance that they should be stable as well as selective. **Figure 5.25** shows the plot of PL intensity of CDs after addition of 100 µM TNP with incubation time of upto 2 h. A sharp decrease in the PL intensity is seen indicating that the quenching process occurred within the first 1 min. The system also exhibited excellent stability upto 120 min.

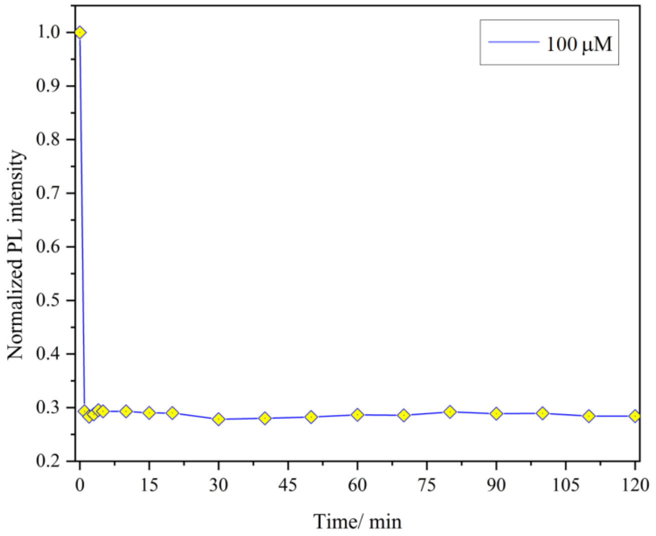

Figure 5.25 Effect of incubation time on the PL quenching of CDs ([C] =100 μM).

For testing the selectivity of the CDs towards TNP, two other NACs *viz.* 2,4-DNP and p-NP were chosen. The PL quenching plots for these two analytes are given in **Figure 5.26 (a)** and

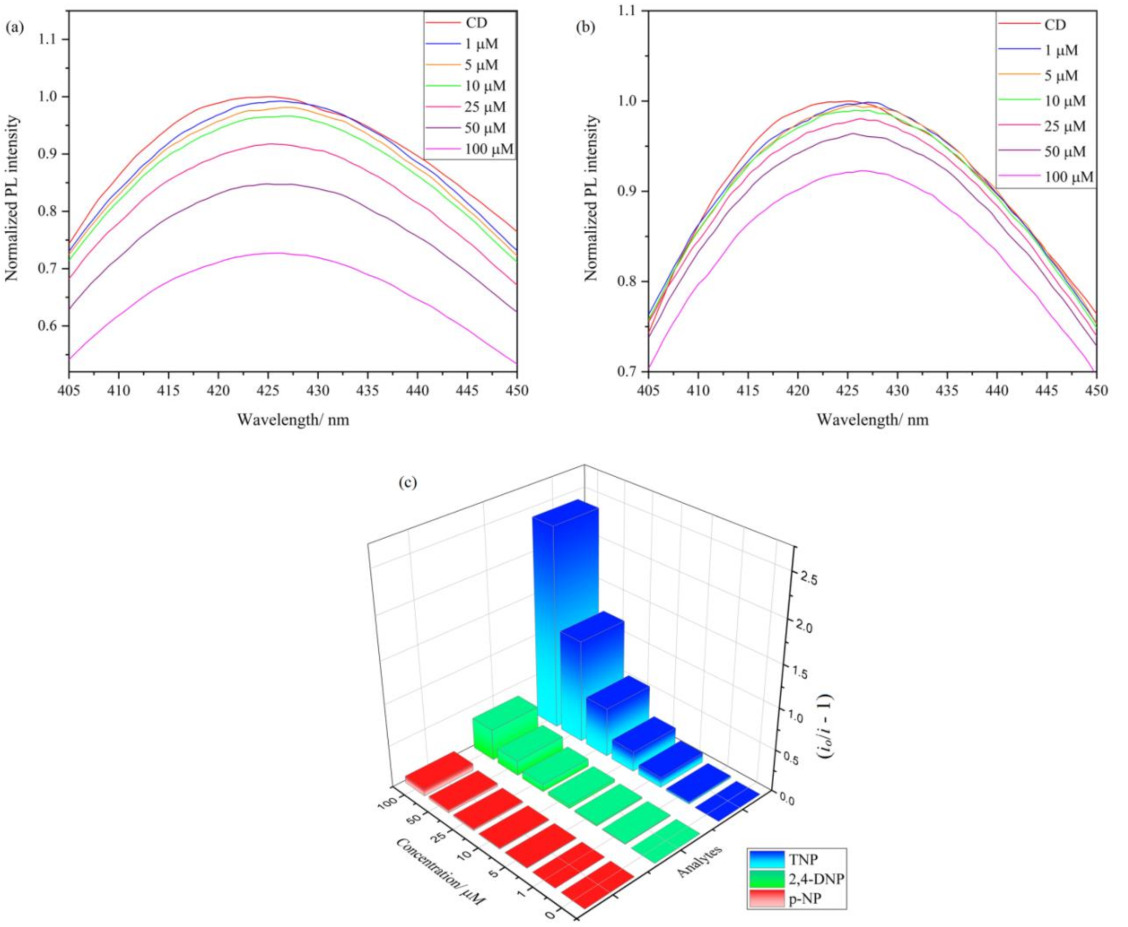

Figure 5.26 Variation of PL emission of CDs with addition of **(a)** 2,4-DNP and **(b)** p-NP, and **(c)** **v**ariation of ((i_o/i)-1) for TNP, 2,4-DNP and p-NP in the linear range from 0-100 μM.

(b).The comparative Stern-Volmer plots of all the three compounds are shown in **Figure 5.26 (c)** and their quenching constants are given in **Table 5.5**. A significantly higher K_{SV} value for TNP suggests that the CDs are predominantly selective towards TNP over others.

Table 5.5 Fluorescence quenching constant (K_{SV}) and correlation values of different analytes.

Analyte	K_{SV}/ M^{-1}	Correlation coefficient
TNP	2.42×10^4	0.9998
2,4-DNP	3.7×10^3	0.9992
p-NP	8.0×10^2	0.9946

In order to explain the PL quenching phenomenon, different mechanisms such as FRET or inner filter effect (IFE) and charge transfer process, etc. have been suggested [86,87]. There is a significant overlap between the emission spectrum of the fluorophore (CDs) and the absorption spectrum of the quencher (TNP) (**Figure 5.27 (a)**), so the condition for IFE is fulfilled and it can be considered as one of the most probable reasons for fluorescence quenching. This phenomenon is further validated when reduced spectral overlap between the emission spectrum of CDs and the absorption spectra of other NACs results in relatively poor detection.

The possibility of a charge transfer process was verified using UV-vis spectroscopy [88]. Upon addition of TNP in the CD solution, increased absorption intensity can be seen at 377 nm due to gradually increasing presence of TNP molecules (**Figure 5.27 (b)**). However, no new peak arises, which excludes the probability of any charge transfer process between the CDs and TNP. In addition, fluorescence can also be quenched by other processes like electrostatic interactions and hydrogen bonding between CDs and TNP, etc. [89]. The prospect of hydrogen bonding was theoretically tested by employing density functional theory (DFT) with basis set B3LYP/6-31+G* [90]. The results simulated with a simple CD structure yielded a hydrogen bond length of 0.142547 nm between O1 of the carboxylic group (of CD) and H1 of the hydroxyl group (of TNP) (**Figure 5.27 (c)**).

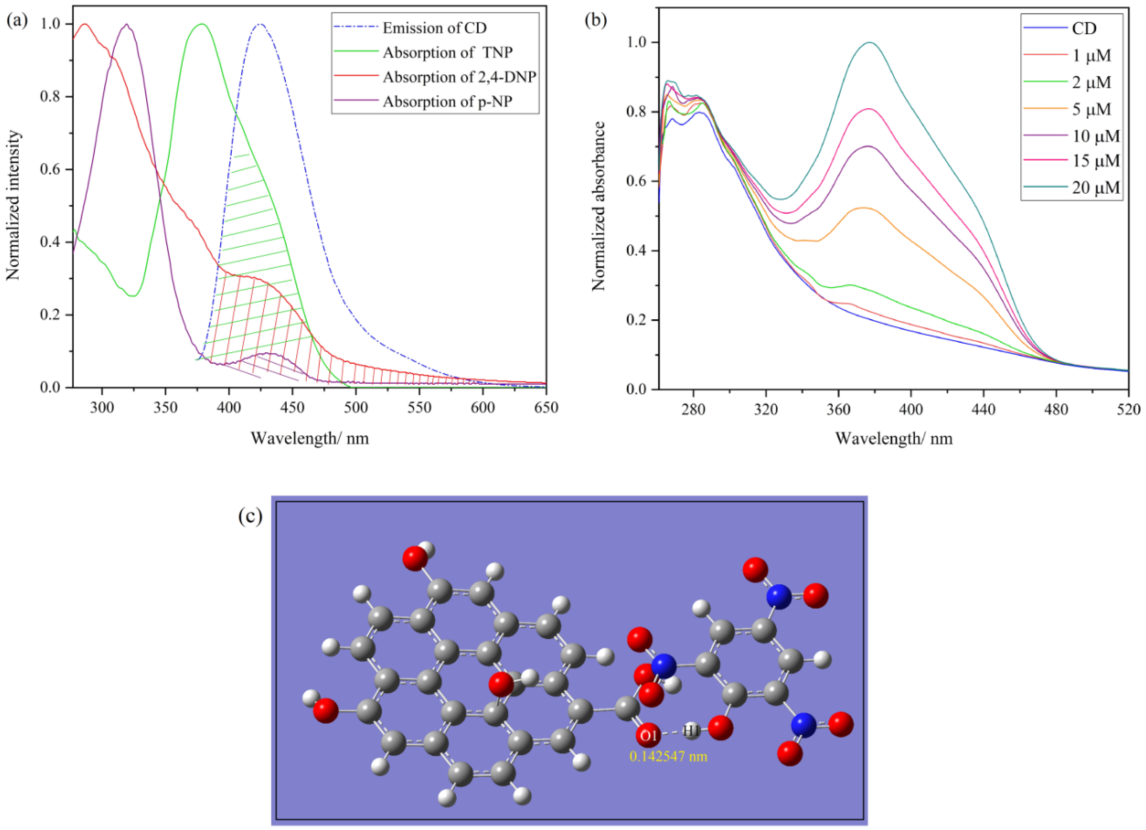

Figure 5.27(a) UV-visible spectra of TNP, 2,4-DNP and p-NP, and their overlap with the CD emission spectrum, **(b)** UV-visible spectra of CDs in the presence of TNP with different concentrations and **(c)** DFT studies of hydrogen bonding interactions of CDs with TNP.

5.13 Conclusion

In conclusion, we have synthesized CDs using solvothermal route from a green carbon sources that has not been previously explored for CD preparation, i.e., gallic acid using DMF as the reaction medium. Elemental analysis reveals the presence of C, O and N, while TEM analysis highlights the amorphous nature of these CDs. Meanwhile, the CDs are very sensitive towards the detection of TNP with a LOD value of 0.75 µM. The fast and selective detection approach is based on the fluorescence quenching behavior of B-CDs in presence of TNP. Overall, we have established a simple strategy for fast synthesis of blue emitting CDs from a new source, and demonstrated their practical application in the area of fluorescence sensor.

5.14 References

[1] Zhang, Y.-Q., Ma, D.-K., Zhang, Y.-G., Chen, W., and Huang, S.-M. N-doped carbon quantum dots for TiO_2-based photocatalysts and dye-sensitized solar cells. *Nano Energy*, 2(5):545-552, 2013.

[2] Mirtchev, P., Henderson, E. J., Soheilnia, N., Yip, C. M., and Ozin, G. A. Solution phase synthesis of carbon quantum dots as sensitizers for nanocrystalline TiO_2 solar cells. *Journal of Materials Chemistry*, 22(4):1265-1269, 2012.

[3] Sachdev, A. and Gopinath, P. Green synthesis of multifunctional carbon dots from coriander leaves and their potential application as antioxidants, sensors and bioimaging agents. *Analyst*, 140(12):4260-4269, 2015.

[4] Bhunia, S. K., Saha, A., Maity, A. R., Ray, S. C., and Jana, N. R. Carbon nanoparticle-based fluorescent bioimaging probes. *Scientific Reports*, 3(1):1473, 2013.

[5] Jiang, K., Sun, S., Zhang, L., Lu, Y., Wu, A., Cai, C., and Lin, H. Red, green, and blue luminescence by carbon dots: Full-color emission tuning and multicolor cellular imaging. *Angewandte Chemie International Edition*, 54(18):5360-5363, 2015.

[6] Zhu, J., Bai, X., Bai, J., Pan, G., Zhu, Y., Zhai, Y., Shao, H., Chen, X., Dong, B., Zhang, H., and Song, H. Emitting color tunable carbon dots by adjusting solvent towards light-emitting devices. *Nanotechnology*, 29(8):085705, 2018.

[7] Qu, D., Zheng, M., Li, J., Xie, Z., and Sun, Z. Tailoring color emissions from N-doped graphene quantum dots for bioimaging applications. *Light: Science & Applications*, 4(12):e364-e364, 2015.

[8] Du, Q., Zheng, J., Wang, J., Yang, Y., and Liu, X. The synthesis of green fluorescent carbon dots for warm white LEDs. *RSC Advances*, 8(35):19585-19595, 2018.

[9] Huang, H., Yang, S., Vajtai, R., Wang, X., and Ajayan, P. M. Pt-decorated 3D architectures built from graphene and graphitic carbon nitride nanosheets as efficient methanol oxidation catalysts. *Advanced Materials*, 26(30):5160-5165, 2014.

[10] Zhao, X., Yin, M., Ma, L., Liang, L., Liu, C., Liao, J., Lu, T., and Xing, W. Recent advances in catalysts for direct methanol fuel cells. *Energy and Environmental Science*, 4(8):2736-2753, 2011.

[11] Zhang, Z., Yuan, Y., Fang, Y., Liang, L., Ding, H., Shi, G., and Jin, L. Photoelectrochemical oxidation behavior of methanol on highly ordered TiO_2 nanotube array electrodes. *Journal of Electroanalytical Chemistry*, 610(2):179-185, 2007.

[12] Song, Y.-Y., Gao, Z.-D., and Schmuki, P. Highly uniform Pt nanoparticle decoration on TiO_2 nanotube arrays: A refreshable platform for methanol electrooxidation. *Electrochemistry Communications*, 13(3):290-293, 2011.

[13] Sui, X.-L., Wang, Z.-B., Xia, Y.-F., Yang, M., Zhao, L., and Gu, D.-M. A rapid synthesis of TiO_2 nanotubes in an ethylene glycol system by anodization as a Pt-based catalyst support for methanol electrooxidation. *RSC Advances*, 5(45):35518-35523, 2015.

[14] Dholam, R., Patel, N., Adami, M., and Miotello, A. Hydrogen production by photocatalytic water-splitting using Cr- or Fe-doped TiO_2 composite thin films photocatalyst. *International Journal of Hydrogen Energy*, 34(13):5337-5346, 2009.

[15] Lee, Y. L., Chi, C. F., and Liau, S. Y. CdS/CdSe Co-Sensitized TiO_2 photoelectrode for efficient hydrogen generation in a photoelectrochemical cell. *Chemistry of Materials*, 22(3):922-927, 2010.

[16] Zhang, J., Du, P., Schneider, J., Jarosz, P., and Eisenberg, R. Photogeneration of hydrogen from water using an integrated system based on TiO_2 and platinum(II) diimine dithiolate sensitizers. *Journal of the American Chemical Society*, 129(25):7726-7727, 2007.

[17] Xie, S., Su, H., Wei, W., Li, M., Tong, Y., and Mao, Z. Remarkable photoelectrochemical performance of carbon dots sensitized TiO_2 under visible light irradiation. *Journal of Materials Chemistry A*, 2(39):16365-16368, 2014.

[18] Hong, T. Z., Xue, Q., Yang, Z. Y., and Dong, Y. P. Great-enhanced performance of Pt nanoparticles by the unique carbon quantum dot/reduced graphene oxide hybrid supports towards methanol electrochemical oxidation. *Journal of Power Sources*, 303:109-117, 2016.

[19] Sun, Y., Zhou, Y., Zhu, C., Hu, L., Han, M., Wang, A., Huang, H., Liu, Y., and Kang, Z. A Pt-Co_3O_4-CD electrocatalyst with enhanced electrocatalytic performance and resistance to CO poisoning achieved by carbon dots and Co_3O_4 for direct methanol fuel cells. *Nanoscale*, 9(17):5467-5474, 2017.

[20] Pan, D., Li, X., and Zhang, A. Platinum assisted by carbon quantum dots for methanol electro-oxidation. *Applied Surface Science*, 427:715-723, 2018.

[21] Zheng, H., Niu, P., and Zhao, Z. Carbon quantum dot sensitized Pt@Bi_2WO_6/FTO electrodes for enhanced photoelectro-catalytic activity of methanol oxidation. *RSC Advances*, 7(43):26943-26951, 2017.

[22] Zhai, C., Zhu, M., Bin, D., Wang, H., Du, Y., Wang, C., and Yang, P. Visible-light-assisted electrocatalytic oxidation of methanol using reduced graphene oxide modified Pt nanoflowers-TiO_2 nanotube arrays. *ACS Applied Materials and Interfaces*, 6(20):17753-17761, 2014.

[23] Zhu, S., Meng, Q., Wang, L., Zhang, J., Song, Y., Jin, H., Zhang, K., Sun, H., Wang, H., and Yang, B. Highly photoluminescent carbon dots for multicolor patterning, sensors, and bioimaging. *Angewandte Chemie - International Edition*, 52(14):3953-3957, 2013.

[24] Yu, H., Zhao, Y., Zhou, C., Shang, L., Peng, Y., Cao, Y., Wu, L.-Z., Tung, C.-H., and Zhang, T. Carbon quantum dots/TiO_2 composites for efficient photocatalytic hydrogen evolution. *Journal of Materials Chemistry A*, 2(10):3344, 2014.

[25] Zhu, S., Meng, Q., Wang, L., Zhang, J., Song, Y., Jin, H., Zhang, K., Sun, H., Wang, H., and Yang, B. Highly photoluminescent carbon dots for multicolor patterning, sensors, and bioimaging. *Angewandte Chemie - International Edition*, 52(14):3953-3957, 2013.

[26] Zhang, H., Lv, X., Li, Y., Wang, Y., and Li, J. P25-graphene composite as a high performance photocatalyst. *ACS Nano*, 4(1):380-386, 2010.

[27] Cui, Y., Zhang, C., Sun, L., Hu, Z., and Liu, X. Simple and efficient synthesis of strongly green fluorescent carbon dots with upconversion property for direct cell imaging. *Particle and Particle Systems Characterization*, 32(5):542-546, 2015.

[28] Zhou, L., Wang, Y., Tang, J., Li, J., Wang, S., and Wang, Y. Facile synthesis of holey graphene-supported Pt catalysts for direct methanol electro-oxidation. *Microporous and Mesoporous Materials*, 247:116-123, 2017.

[29] Du, F., Yuan, J., Zhang, M., Li, J., Zhou, Z., Li, Z., Cao, M., Chen, J., Zhang, L., Liu, X., Gong, A., Xu, W., and Shao, Q. Nitrogen-doped carbon dots with heterogeneous multi-layered structures. *RSC Advances*, 4(71):37536-37541, 2014.

[30] Xia, B. Y., Wang, B., Wu, H. Bin, Liu, Z., Wang, X., and Lou, X. W. Sandwich-structured TiO_2-Pt-graphene ternary hybrid electrocatalysts with high efficiency and stability. *Journal of Materials Chemistry*, 22(32):16499-16505, 2012.

[31] Lin, J., Wang, B., Sproul, W. D., Ou, Y., and Dahan, I. Anatase and rutile TiO_2 films deposited by arc-free deep oscillation magnetron sputtering. *Journal of Physics D: Applied Physics*, 46(8):084008, 2013.

[32] Xiang, X., He, W., Xie, L., and Li, F. A mild solution chemistry method to synthesize hydrotalcite-supported platinum nanocrystals for selective hydrogenation of cinnamaldehyde in neat water. *Catalysis Science and Technology*, 3(10):2819-2827, 2013.

[33] Wang, Y., Kalytchuk, S., Zhang, Y., Shi, H., Kershaw, S. V., and Rogach, A. L. Thickness-dependent full-color emission tunability in a flexible carbon dot ionogel. *The Journal of Physical Chemistry Letters*, 5(8):1412-1420, 2014.

[34] Suzuki, K., Malfatti, L., Takahashi, M., Carboni, D., Messina, F., Tokudome, Y., Takemoto, M., and Innocenzi, P. Design of carbon dots photoluminescence through organo-functional silane grafting for solid-state emitting devices. *Scientific Reports*, 7(1):5469, 2017.

[35] Luttrell, T., Halpegamage, S., Tao, J., Kramer, A., Sutter, E., and Batzill, M. Why is anatase a better photocatalyst than rutile? - Model studies on epitaxial TiO_2 films.

Scientific Reports, 4(1):4043, 2015.

[36] Tauc, J. Absorption edge and internal electric fields in amorphous semiconductors. *Materials Research Bulletin*, 5(8):721-729, 1970.

[37] Bao, L., Lin, Y., Qi, B., Tian, Z.-Q., Zhang, Z.-L., Pang, D.-W., Zhang, L., and Liu, C. Electrochemical tuning of luminescent carbon nanodots: From preparation to luminescence mechanism. *Advanced Materials*, 23(48):5801-5806, 2011.

[38] Li, H., He, X., Kang, Z., Huang, H., Liu, Y., Liu, J., Lian, S., Tsang, C. H. A., Yang, X., and Lee, S. T. Water-soluble fluorescent carbon quantum dots and photocatalyst design. *Angewandte Chemie - International Edition*, 49(26):4430-4434, 2010.

[39] Vilian, A. T. T. E., Hwang, S. K., Kwak, C. H., Oh, S. Y., Kim, C. Y., Lee, G. W., Lee, J. B., Huh, Y. S., and Han, Y. K. Pt-Au bimetallic nanoparticles decorated on reduced graphene oxide as an excellent electrocatalysts for methanol oxidation. *Synthetic Metals*, 219:52-59, 2016.

[40] Pal, A., Sk, M. P., and Chattopadhyay, A. Conducting carbon dot-polypyrrole nanocomposite for sensitive detection of picric acid. *ACS Applied Materials and Interfaces*, 8(9):5758-5762, 2016.

[41] Mancharan, R. and Goodenough, J. B. Methanol oxidation in acid on ordered NiTi. *Journal of Materials Chemistry*, 2(8):875, 2004.

[42] Zhu, J., Huang, S., Key, J., Nie, S., Ma, S., and Shen, P. K. Facile synthesis of a molybdenum phosphide (MoP) nanocomposite Pt support for high performance methanol oxidation. *Catalysis Science and Technology*, 7(24):5974-5981, 2017.

[43] Holstein, W. L. and Rosenfeld, H. D. In-situ X-ray absorption spectroscopy study of Pt and Ru chemistry during methanol electrooxidation. *The Journal of Physical Chemistry B*, 109(6):2176-2186, 2005.

[44] Gilman, S. The mechanism of electrochemical oxidation of carbon monoxide and methanol on platinum. II. The “reactant-pair” mechanism for electrochemical oxidation of carbon monoxide and methanol. *The Journal of Physical Chemistry*, 68:70-80, 1964.

[45] Ahmed, A. Y., Kandiel, T. A., Ivanova, I., and Bahnemann, D. Photocatalytic and photoelectrochemical oxidation mechanisms ofmethanol on TiO_2 in aqueous solution. *Applied Surface Science*, 319(1):44-49, 2014.

[46] Ahmed, A. Y., Kandiel, T. A., Oekermann, T., and Bahnemann, D. Photocatalytic activities of different well-defined single crystal TiO_2 surfaces: Anatase versus rutile. *The Journal of Physical Chemistry Letters*, 2(19):2461-2465, 2011.

[47] Schneider, J., Matsuoka, M., Takeuchi, M., Zhang, J., Horiuchi, Y., Anpo, M., and Bahnemann, D. W. Understanding TiO_2 photocatalysis: Mechanisms and materials. *Chemical Reviews*, 114(19):9919-9986, 2014.

[48] Xu, A.-W., Gao, Y., and Liu, H.-Q. The preparation, characterization, and their photocatalytic activities of rare-earth-doped TiO_2 nanoparticles. *Journal of Catalysis*, 207(2):151-157, 2002.

[49] Chen, C.-S. and Pan, F.-M. Electrocatalytic activity of Pt nanoparticles deposited on porous TiO_2 supports toward methanol oxidation. *Applied Catalysis B: Environmental*, 91(3):663-669, 2009.

[50] Sharma, S., Groves, M. N., Fennell, J., Soin, N., Horswell, S. L., and Malardier-Jugroot, C. Carboxyl group enhanced CO tolerant GO supported Pt catalysts: DFT and electrochemical analysis. *Chemistry of Materials*, 26(21):6142-6151, 2014.

[51] Ke, J., Li, X., Zhao, Q., Liu, B., Liu, S., and Wang, S. Upconversion carbon quantum dots as visible light responsive component for efficient enhancement of photocatalytic performance. *Journal of Colloid and Interface Science*, 496:425-433, 2017.

[52] Sun, M., Ma, X., Chen, X., Sun, Y., Cui, X., and Lin, Y. A nanocomposite of carbon quantum dots and TiO_2 nanotube arrays: Enhancing photoelectrochemical and photocatalytic properties. *RSC Advances*, 4(3):1120-1127, 2014.

[53] Gong, J., Liang, J., and Sumathy, K. Review on dye-sensitized solar cells (DSSCs): Fundamental concepts and novel materials. *Renewable and Sustainable Energy Reviews*, 16(8):5848-5860, 2012.

[54] Li, Z. Q., Chen, W. C., Guo, F. L., Mo, L. E., Hu, L. H., and Dai, S. Y. Mesoporous TiO_2 yolk-shell microspheres for dye-sensitized solar cells with a high efficiency exceeding 11%. *Scientific Reports*, 5(1):14178, 2015.

[55] Hirata, N., Lagref, J. J., Palomares, E. J., Durrant, J. R., Nazeeruddin, M. K., Gratzel, M., and Di Censo, D. Supramolecular control of charge-transfer dynamics on dye-sensitized nanocrystalline TiO_2 films. *Chemistry - A European Journal*, 10(3):595-602, 2004.

[56] Huang, J. J., Zhong, Z. F., Rong, M. Z., Zhou, X., Chen, X. D., and Zhang, M. Q. An easy approach of preparing strongly luminescent carbon dots and their polymer based composites for enhancing solar cell efficiency. *Carbon*, 70:190-198, 2014.

[57] Paulo, S., Palomares, E., and Martinez-Ferrero, E. Graphene and carbon quantum dot-based materials in photovoltaic devices: From synthesis to applications. *Nanomaterials*, 6(9):157, 2016.

[58] Tang, Q., Zhu, W., He, B., and Yang, P. Rapid conversion from carbohydrates to large-scale carbon quantum dots for all-weather solar cells. *ACS Nano*, 11(2):1540-1547, 2017.

[59] Zhao, Y., Duan, J., He, B., Jiao, Z., and Tang, Q. Improved charge extraction with N-doped carbon quantum dots in dye-sensitized solar cells. *Electrochimica Acta*, 282:255-262, 2018.

[60] Mohan, K., Bora, A., and Dolui, S. K. Efficient way of enhancing the efficiency of a

quasi-solid-state dye-sensitized solar cell by harvesting the unused higher energy visible light using carbon dots. *ACS Sustainable Chemistry and Engineering*, 6(8):10914-10922, 2018.

[61] Sahu, S., Behera, B., Maiti, T. K., and Mohapatra, S. Simple one-step synthesis of highly luminescent carbon dots from orange juice: Application as excellent bio-imaging agents. *Chemical Communications*, 48(70):8835-8837, 2012.

[62] Guo, Y., Wang, Z., Shao, H., and Jiang, X. Hydrothermal synthesis of highly fluorescent carbon nanoparticles from sodium citrate and their use for the detection of mercury ions. *Carbon*, 52:583-589, 2013.

[63] Ding, H., Yu, S. B., Wei, J. S., and Xiong, H. M. Full-color light-emitting carbon dots with a surface-state-controlled luminescence mechanism. *ACS Nano*, 10(1):484-491, 2016.

[64] Dong, Y., Pang, H., Yang, H. Bin, Guo, C., Shao, J., Chi, Y., Li, C. M., and Yu, T. Carbon-based dots co-doped with nitrogen and sulfur for high quantum yield and excitation-independent emission. *Angewandte Chemie - International Edition*, 52(30):7800-7804, 2013.

[65] Sekiya, R., Uemura, Y., Naito, H., Naka, K., and Haino, T. Chemical functionalisation and photoluminescence of graphene quantum dots. *Chemistry - A European Journal*, 22(24):8198-8206, 2016.

[66] Zeng, Z., Zhang, W., Arvapalli, D. M., Bloom, B., Sheardy, A., Mabe, T., Liu, Y., Ji, Z., Chevva, H., Waldeck, D. H., and Wei, J. A fluorescence-electrochemical study of carbon nanodots (CNDs) in bio- and photoelectronic applications and energy gap investigation. *Physical Chemistry Chemical Physics*, 19(30):20101-20109, 2017.

[67] Lee, C. P., Yeh, M. H., Vittal, R., and Ho, K. C. Solid-state dye-sensitized solar cell with a charge transfer layer comprising two ionic liquids and a carbon material. *Journal of Materials Chemistry*, 21(39):15471-15478, 2011.

[68] Zhang, Y. Q., Ma, D. K., Zhang, Y. G., Chen, W., and Huang, S. M. N-doped carbon quantum dots for TiO_2 -based photocatalysts and dye-sensitized solar cells. *Nano Energy*, 2(5):545-552, 2013.

[69] Sun, M., Ma, X., Chen, X., Sun, Y., Cui, X., and Lin, Y. A nanocomposite of carbon quantum dots and TiO_2 nanotube arrays: Enhancing photoelectrochemical and photocatalytic properties. *RSC Advances*, 4(3):1120-1127, 2014.

[70] Briscoe, J., Marinovic, A., Sevilla, M., Dunn, S., and Titirici, M. Biomass-derived carbon quantum dot sensitizers for solid-state nanostructured solar cells. *Angewandte Chemie - International Edition*, 54(15):4463-4468, 2015.

[71] Ma, Z., Zhang, Y. L., Wang, L., Ming, H., Li, H., Zhang, X., Wang, F., Liu, Y., Kang, Z.,

and Lee, S. T. Bioinspired photoelectric conversion system based on carbon-quantum-dot- doped dye-semiconductor complex. *ACS Applied Materials and Interfaces*, 5(11):5080-5084, 2013.

[72] *Picric acid - National Library of Medicine HSDB Database*. Retrieved on 5 Jun. 2019 from https://toxnet.nlm.nih.gov/cgi-bin/sis/search/a?dbs+hsdb:@term+@DOCNO+2040, June 2019.

[73] Zhu, M., Wu, X., Niu, B., Guo, H., and Zhang, Y. Fluorescence sensing of 2,4,6-trinitrophenol based on hierarchical IRMOF-3 nanosheets fabricated through a simple one-pot reaction. *Applied Organometallic Chemistry*, 32(5):e4333, 2018.

[74] Peng, Y., Zhang, A. J., Dong, M., and Wang, Y. W. A colorimetric and fluorescent chemosensor for the detection of an explosive-2,4,6-trinitrophenol (TNP). *Chemical Communications*, 47(15):4505-4507, 2011.

[75] Nagarkar, S. S., Joarder, B., Chaudhari, A. K., Mukherjee, S., and Ghosh, S. K. Highly selective detection of nitro explosives by a luminescent metal-organic framework. *Angewandte Chemie - International Edition*, 52(10):2881-2885, 2013.

[76] Na, W., Liu, X., Pang, S., and Su, X. Highly sensitive detection of 2,4,6-trinitrophenol (TNP) based on lysozyme capped CdS quantum dots. *RSC Advances*, 5(63):51428-51434, 2015.

[77] Wang, X., Cao, L., Lu, F., Meziani, M. J., Li, H., Qi, G., Zhou, B., Harruff, B. A., Kermarrec, F., and Sun, Y. P. Photoinduced electron transfers with carbon dots. *Chemical Communications*, (25):3774-3776, 2009.

[78] Niu, Q., Gao, K., Lin, Z., and Wu, W. Amine-capped carbon dots as a nanosensor for sensitive and selective detection of picric acid in aqueous solution via electrostatic interaction. *Analytical Methods*, 5(21):6228-6233, 2013.

[79] Ren, G., Yu, L., Zhu, B., Tang, M., Chai, F., Wang, C., and Su, Z. Orange emissive carbon dots for colorimetric and fluorescent sensing of 2,4,6-trinitrophenol by fluorescence conversion. *RSC Advances*, 8(29):16095-16102, 2018.

[80] Shi, D., Yan, F., Zheng, T., Wang, Y., Zhou, X., and Chen, L. P-doped carbon dots act as a nanosensor for trace 2,4,6-trinitrophenol detection and a fluorescent reagent for biological imaging. *RSC Advances*, 5(119):98492-98499, 2015.

[81] Cheng, F., An, X., Zheng, C., and Cao, S. Green synthesis of fluorescent hydrophobic carbon quantum dots and their use for 2,4,6-trinitrophenol detection. *RSC Advances*, 5(113):93360-93363, 2015.

[82] Du, Q., Zheng, J., Wang, J., Yang, Y., and Liu, X. The synthesis of green fluorescent carbon dots for warm white LEDs. *RSC Advances*, 8(35):19585-19595, 2018.

[83] Joseph, J. and Anappara, A. A. Microwave-assisted hydrothermal synthesis of UV-

emitting carbon dots from tannic acid. *New Journal of Chemistry*, 40(9):8110-8117, 2016.

[84] Huang, Z., Shen, Y., Li, Y., Zheng, W., Xue, Y., Qin, C., Zhang, B., Hao, J., and Feng, W. Facile synthesis of analogous graphene quantum dots with sp^2 hybridized carbon atom dominant structures and their photovoltaic application. *Nanoscale*, 6(21):13043-13052, 2014.

[85] Du, F., Yuan, J., Zhang, M., Li, J., Zhou, Z., Li, Z., Cao, M., Chen, J., Zhang, L., Liu, X., Gong, A., Xu, W., and Shao, Q. Nitrogen-doped carbon dots with heterogeneous multi-layered structures. *RSC Advances*, 4(71):37536-37541, 2014.

[86] Siddique, A. B., Pramanick, A. K., Chatterjee, S., and Ray, M. Amorphous carbon dots and their remarkable ability to detect 2,4,6-trinitrophenol. *Scientific Reports*, 8(1):9770, 2018.

[87] Sun, X. and Lei, Y. Fluorescent carbon dots and their sensing applications. *TrAC - Trends in Analytical Chemistry*, 89:163-180, 2017.

[88] Hughes, S., Dasary, S. S. R., Begum, S., Williams, N., and Yu, H. Meisenheimer complex between 2,4,6-trinitrotoluene and 3-aminopropyltriethoxysilane and its use for a paper-based sensor. *Sensing and Bio-Sensing Research*, 5:37-41, 2015.

[89] Rong, M., Lin, L., Song, X., Zhao, T., Zhong, Y., Yan, J., Wang, Y., and Chen, X. A label-free fluorescence sensing approach for selective and sensitive detection of 2,4,6-trinitrophenol (TNP) in aqueous solution using graphitic carbon nitride nanosheets. *Analytical Chemistry*, 87(2):1288-1296, 2015.

[90] Xue, H., Yan, Y., Hou, Y., Li, G., and Hao, C. Novel carbon quantum dots for fluorescent detection of phenol and insights into the mechanism. *New Journal of Chemistry*, 42(14):11485-11492, 2018.